Many-body theory of electron scattering by excited atomic targets: Electron-impact-induced transitions $2\,^{1,3}S \rightarrow n\,^{1,3}L$ ($L=0,1,2$; $n=2,3,4$) in helium

David C. Cartwright and G. Csanak
Los Alamos National Laboratory, Los Alamos, New Mexico 87545
(Received 11 July 1994)

A many-body-theory (MBT) formulation for electron scattering by excited electronic states is applied to excitation from the $2\,^{1,3}S$ metastable states of helium. The lowest-order MBT for these transitions involves a "chanel coupling" to the ground state of helium as well as a distortion of the free-electron wave function by the ground state of the target, while the distorted-wave approximation (DWA) involves a distortion of the incident and scattered electron wave functions by the initial and final target states, respectively. Results using the first-order many-body theory and DWA are reported here for integral and differential cross sections for excitation from the $2\,^{1,3}S$ states to (2,3) $^{1,3}P$, $3\,^{1,3}S$, and $3\,^{1,3}D$ states, and are compared with published experimental and theoretical data.

PACS number(s): 34.80.Dp

I. INTRODUCTION

In the first paper in this series [1], hereafter referred to as paper I, a many-body theory (MBT) for the description of electron-impact excitation from excited states of atomic systems with closed-shell ground states was presented. The first-order version of the general theory, called first-order many-body theory (FOMBT), was detailed [1] by performing angular momentum and spin analyses on quantities that enter the fundamental equations and formulas of FOMBT. In this paper, results from application of FOMBT to treat electron-impact excitation out of the metastable $2\,^{1,3}S$ states in helium is reported.

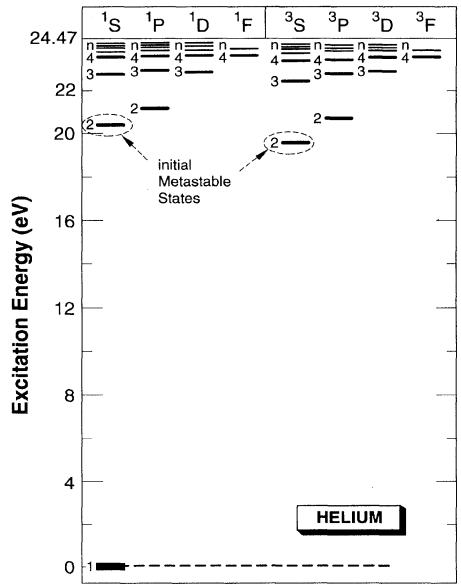

FIG. 1. Energy-level diagram for atomic helium. Electron-impact excitation from the two metastable states ($2\,^{1,3}S$ shown enclosed in dashed ellipses) to the higher $n=2$ and all $n=3$ states is the subject of this paper.

An energy-level diagram for helium is shown in Fig. 1 in which the lowest two $n=2$ states are the metastable $2\,^{1,3}S$ initial states. In this work, single-configuration approximations for the ground- and excited-state wave functions of He were used. Introducing this class of He wave functions results in relatively simple approximate expressions for the transition density matrices that are used in the fundamental equations and formulas of FOMBT presented in paper I. This paper reports results from applying FOMBT and a distorted-wave approximation (DWA) to those transitions from the $2\,^{1,3}S$ metastable states for which experimental results and/or results from other theories have been reported. The DWA used in this work was obtained by selectively summing an infinite number of initial- and final-state distortion diagrams as discussed in paper I. Systematics in these cross sections and extrapolation of the excitation cross sections to obtain an estimate of the total cross section for excitation to all bound states in helium will be presented in a subsequent paper.

II. WAVE FUNCTIONS AND TRANSITION DENSITY MATRICES FOR HELIUM

A. Ground-to-excited-state density matrix

The ground-to-excited-state transition density matrix was defined in paper I [see Eq. (25a) in I] by the formula (the general notation in paper I will be used here)

$$X_n(\mathbf{r}\sigma,\mathbf{r}'\sigma')=\langle\Psi_0|\psi^\dagger(\mathbf{r}\sigma)\psi(\mathbf{r}'\sigma')|\Psi_n\rangle\ , \tag{1}$$

which can also be expressed in terms of the ground-state $[\Psi_0(\mathbf{r}_1\sigma_1,\ldots,\mathbf{r}_N\sigma_N)]$ and excited-state $[\Psi_n(\mathbf{r}_1\sigma_1,\ldots,\mathbf{r}_N\sigma_N)]$ wave functions for the general N-electron system in the form

$$X_n(\mathbf{r}\sigma,\mathbf{r}'\sigma')=N\int d\mathbf{r}_2 d\sigma_2\cdots d\mathbf{r}_N d\sigma_N \times\Psi_0^*(\mathbf{r}\sigma,\mathbf{r}_2\sigma_2,\ldots,\mathbf{r}_N\sigma_N) \times\Psi_n(\mathbf{r}'\sigma',\mathbf{r}_2\sigma_2,\ldots,\mathbf{r}_N\sigma_N)\ . \tag{2}$$

1. Transitions not involving an $n\,{}^1S$ state

For transition that do not involve an $n\,{}^1S$ excited state in Eq. (2), reasonable accuracy is obtained for the transition density matrix by using the Hartree-Fock (HF) wave function for the ground state and the "fixed-core" HF wave functions for the excited states [2]. For the ground-state wave function, the form is

$$\Psi_0(\mathbf{r}_1\sigma_1,\mathbf{r}_2\sigma_2) = \varphi_{1s}(\mathbf{r}_1)\varphi_{1s}(\mathbf{r}_2)\frac{1}{\sqrt{2}}\{\alpha(\sigma_1)\beta(\sigma_2)-\beta(\sigma_1)\alpha(\sigma_2)\} , \tag{3}$$

where $\varphi_{1s}(\mathbf{r})$ is the spatially normalized HF $1s$ orbital of He, which satisfies

$$\int d\mathbf{r}|\varphi_{1s}(\mathbf{r})|^2=1 , \tag{4}$$

and α and β are the Pauli spin functions. For the excited-state wave functions (other than $n\,{}^1S$), form is

$$\Psi_n(\mathbf{r}_1\sigma_1,\mathbf{r}_2\sigma_2)=\frac{1}{\sqrt{2(1\pm|S_{1s,n}|^2)}} \times\{\varphi_{1s}(\mathbf{r}_1)\varphi_n(\mathbf{r}_2)\pm\varphi_{1s}(\mathbf{r}_2)\varphi_n(\mathbf{r}_1)\} \times S_{S^nM_S^n}(\sigma_1\sigma_2) , \tag{5}$$

where $\varphi_n(\mathbf{r})$ is the spatially normalized fixed-core HF orbital, $S_{S^nM_S^n}(\sigma_1\sigma_2)$ refers to the two-electron spin function defined by the formula

$$S_{S^nM_S^n}(\sigma_1\sigma_2)=\sum_{m_{s_1},m_{s_2}} C^{1/2\ \ 1/2\ \ S^n}_{m_{s_1}\ m_{s_2}\ M_S^n}\eta_{m_{s_1}}(\sigma_1)\eta_{m_{s_2}}(\sigma_2) . \tag{6}$$

$\eta_{m_S}(\sigma_1)$ is the Pauli spin function, the minus sign refers to an excited state of overall triplet symmetry, and the plus sign to one of singlet symmetry. The quantity

$$S_{1s,n}=\int d\mathbf{r}\,\varphi^*_{1s}(\mathbf{r})\varphi_n(\mathbf{r}) \tag{7}$$

is the spatial overlap of the φ_{1s} and φ_n orbitals. Substituting these expressions for the ground-state and excited-state wave functions into Eq. (2) for the transition density matrix, one obtains

$$X_n(\mathbf{r}\sigma,\mathbf{r}'\sigma')=\frac{1}{2\sqrt{1\pm|S_{1s,n}|^2}} \times[\pm\varphi^*_{1s}(\mathbf{r})\varphi_{1s}(\mathbf{r}')S_{1s,n} +\varphi^*_{1s}(\mathbf{r})\varphi_n(\mathbf{r}')]\xi_{S^nM_S^n}(\sigma\sigma') , \tag{8}$$

where

$$\xi_{S,M_S}(\sigma\sigma')=\sum_{m_1,m_2}(-1)^{(1/2)+m_1}C^{1/2\ \ 1/2\ \ S}_{-m_1\ \ m_2\ \ M_S} \times\eta^*_{m_1}(\sigma)\eta_{m_2}(\sigma') \tag{9}$$

is the spin function introduced in paper I. If n refers to a ${}^1L$ ($L=P,D,\ldots$) or to a ${}^3L$ ($L=P,D,\ldots$) state, then the overlap integral $S_{1s,n}=0$ because of the different angular parts for the excited-state orbitals. If n refers to a ${}^3S$ state, the fixed-core HF orbital (φ_n) can, if so desired, be made orthogonal [3] to φ_{1s}; but this restriction was not employed here. The expression for the transition density matrix for these cases becomes

$$X_n(\mathbf{r}\sigma,\mathbf{r}'\sigma')=\tfrac{1}{2}\varphi^*_{1s}(\mathbf{r})\bar{\varphi}_n(\mathbf{r}')\xi_{S^nM_S^n}(\sigma\sigma') , \tag{10}$$

where

$$\bar{\varphi}_n(\mathbf{r}')=\frac{1}{\sqrt{1\pm|S_{1s,n}|^2}}[\pm\varphi_{1s}(\mathbf{r}')S_{1s,n}+\varphi_n(\mathbf{r}')] . \tag{11}$$

Introducing the customary angular factorizations for the φ_{1s} and φ_n orbitals

$$\varphi_{1s}(\mathbf{r})=R_{1s}(r)Y_{00}(\hat{\mathbf{r}}) , \tag{12a}$$

$$\varphi_n(\mathbf{r})=R_n(r)Y_{L^nM_L^n}(\hat{\mathbf{r}}) \tag{12b}$$

[see Eq. (53) of paper I], the radial part of the transition density matrix becomes

$$X_n(rr')=R_{1s}(r)\bar{R}_n(r') \tag{13}$$

with

$$\bar{R}_n(r)=\frac{1}{\sqrt{1\pm|S_{1s,n}|^2}}[R_n(r)-S_{1s,n}R_{1s}(r)] . \tag{14}$$

This is the expression that will be used in all equations and formulas of the FOMBT introduced in paper I.

A corresponding expression for $\tilde{X}_n(\mathbf{r}\mathbf{r}')$ can be obtained by using the identity [see Eq. (41) in I]

$$\tilde{X}_n(\mathbf{r}\mathbf{r}')=(-1)^{S^n}X^*_n(\mathbf{r}'\mathbf{r}) , \tag{15}$$

which, by using Eqs. (10)–(12), yields

$$\tilde{X}_n(\mathbf{r}\mathbf{r}')=(-1)^{S^n}\bar{\varphi}^*_n(\mathbf{r})\varphi_{1s}(\mathbf{r}') , \tag{16}$$

$$\tilde{X}_n(\mathbf{r}\mathbf{r}')=\tilde{X}_n(rr')Y^*_{L^nM_L^n}(\hat{\mathbf{r}})Y_{00}(\hat{\mathbf{r}}') , \tag{17}$$

with

$$\tilde{X}_n(\mathbf{r}\mathbf{r}')=(-1)^{S^n}\bar{R}^*_n(r)R_{1s}(r') . \tag{18}$$

2. Transition involving an $n\,{}^1S$ state

When an excited ${}^1S$ state is involved in Eq. (2), the usual fixed-core HF approximation fails because it is of the same symmetry as the ground state. However, a practical and accurate representation for such states has been introduced by McEachran and co-workers [4–6] in which the singlet states of helium are described by the wave functions

$$\Psi_{\bar{n}^1LM_L}(x_1,x_2)=N_{\bar{n}LM_L}[\varphi_0(\mathbf{r}_1)\varphi_{\bar{n}LM_L}(\mathbf{r}_2) +\varphi_0(\mathbf{r}_2)\varphi_{\bar{n}LM_L}(\mathbf{r}_1)] \times\frac{1}{\sqrt{2}}[\alpha(\sigma_1)\beta(\sigma_2)-\beta(\sigma_1)\alpha(\sigma_2)] , \tag{19}$$

where $N_{\bar{n}L}$ is a normalization constant and $\varphi_0(\mathbf{r})$ is the normalized $1s$ orbital of He^+ given by (using hartree atomic units),

$$\varphi_0(\mathbf{r})=2^{5/2}e^{-2r}Y_{00}(\mathbf{r}) . \tag{20}$$

The $\varphi_{\bar{n}LM_L}(\mathbf{r})$ orbitals were obtained by Cohen and McEachran [4] by first solving the fixed core HF equations, with $\varphi_0(\mathbf{r})$ being fixed as given by Eq. (20), and then fitting the $\varphi_{\bar{n}LM_L}(\mathbf{r})$ orbitals numerically to

$$\varphi_{\bar{n}LM_L}(\mathbf{r})=\sum_{n=L+1}^{J-L} B_N^{\bar{n}L}e^{-\beta r}r^{N-1}Y_{LM_L}(\hat{\mathbf{r}}) , \tag{21}$$

and tabulating the $B_N^{\bar{n}L}$ coefficients for $\bar{n}=1$, 2, and 3 with $\beta=1$, $\frac{1}{2}$, and $\frac{1}{3}$, respectively. [It is noted here that the Cohen-McEachran [4] scheme also gives the $1\,^1S$ ground state in the form given by Eq. (19) (with $\bar{n}=1$ and $L=M_L=0$).] The normalization constant in Eq. (19) is given by

$$N_{\bar{n}L}=[2(1+|S_{\bar{n}L,0}|^2)]^{-1/2} , \tag{22}$$

where

$$S_{\bar{n}L,0}=\int d\mathbf{r}\,\varphi^*_{\bar{n}LM_L}(\mathbf{r})\varphi_0(\mathbf{r}) \tag{23}$$

is the usual overlap integral.

Inserting the wave functions given by Eqs. (19) and (20) into Eq. (2) yields

$$X_{\bar{n}\,^1S}(\mathbf{r}\sigma,\mathbf{r}'\sigma')=N_{1S}N_{\bar{n}S}\{\varphi_0(\mathbf{r})\varphi^*_{\bar{n}s}(\mathbf{r}')S_{0,1s}+\varphi_{1s}(\mathbf{r})\varphi^*_0(\mathbf{r}')S_{0,\bar{n}s}+\varphi_{1s}(\mathbf{r})\varphi^*_{\bar{n}s}(\mathbf{r}')\}[\alpha^*(\sigma')\alpha(\sigma)+\beta^*(\sigma')\beta(\sigma)] , \tag{24}$$

where

$$S_{0,\bar{n}s}=\int \varphi^*_0(\mathbf{r}_2)\varphi_{\bar{n}s}(\mathbf{r}_2)d\mathbf{r}_2 . \tag{25}$$

Assuming

$$S_{0,\bar{n}s}=0 \quad \text{for } n>1 , \tag{26}$$

Eq. (24) becomes

$$\begin{aligned}X_{\bar{n}\,^1S}(\mathbf{r}\sigma,\mathbf{r}'\sigma')&=N_{1S}N_{\bar{n}S}\{\varphi_{1s}(\mathbf{r})\varphi^*_{\bar{n}s}(\mathbf{r}')S_{0,1s}+\varphi_{1s}(\mathbf{r})\varphi^*_{\bar{n}s}(\mathbf{r}')\}[\alpha^*(\sigma')\alpha(\sigma)+\beta^*(\sigma')\beta(\sigma)]\\&=N_{1S}N_{\bar{n}S}(1+S_{0,1s})\varphi_{1s}(\mathbf{r})\varphi^*_{\bar{n}s}(\mathbf{r}')[\alpha^*(\sigma')\alpha(\sigma)+\beta^*(\sigma')\beta(\sigma)]\\&\approx\tfrac{1}{2}(1+S^2_{0,1s})^{1/2}\varphi_{1s}(\mathbf{r})\varphi^*_{\bar{n}s}(\mathbf{r}')[\alpha^*(\sigma')\alpha(\sigma)+\beta^*(\sigma')\beta(\sigma)]\\&\equiv\frac{1}{\sqrt{2}}C_{1s}\varphi_{1s}(\mathbf{r})\varphi^*_{\bar{n}s}(\mathbf{r}')[\alpha^*(\sigma')\alpha(\sigma)+\beta^*(\sigma')\beta(\sigma)] .\end{aligned} \tag{27}$$

A practical advantage associated with the use Eq. (27) is that the orthogonality of the $1\,^1S$ and $n\,^1S$ states, expressed by the identity

$$\int X_n(\mathbf{r}\sigma,\mathbf{r}\sigma)d\mathbf{r}\,d\sigma=0 , \tag{28}$$

is preserved. This occurs because both the φ_{1s} and $\varphi_{\bar{n}s}$ orbitals are obtained from the same eigenvalue equation with differing eigenvalues and are therefore orthogonal to each other. Equation (27) shows that even for the $n\,^1S$ states of helium, a single-term, spin-space factorized representation of $X_n(r,r')$ can be obtained if the functions are properly chosen. In the results reported here, the form given by Eq. (27) was used and the $\varphi_{1s}(\mathbf{r})$ and $\varphi_{\bar{n}s}(\mathbf{r})$ orbitals were obtained from the fixed-core HF program of Bates [7] [keeping the $\varphi_0(\mathbf{r})$ orbital fixed].

B. Excited-state to excited-state transition density matrices

The following outlines approximations to the excited-state to excited-state transition densities $X_n^m(r,r')$, as defined by Eq. (25c) in I, to obtain expressions used in the computations.

1. *No ^1S state involved*

When neither m nor n refers to a ^1S excited state of He, the states can be approximated by fixed-core HF wave functions of the form

$$\begin{aligned}\Psi_m(\mathbf{r}_1\sigma_1,\mathbf{r}_2\sigma_2)=&\frac{1}{\sqrt{2(1-|S_{1s,m}|^2)}}\\&\times\{\varphi_{1s}(\mathbf{r}_1)\varphi_m(\mathbf{r}_2)-\varphi_{1s}(\mathbf{r}_2)\varphi_m(\mathbf{r}_1)\}\\&\times S_{S^mM_S^m}(\sigma_1\sigma_2) ,\end{aligned} \tag{29}$$

where $S^m=1$ and $L^m=0$ [since $\varphi_m(\mathbf{r})$ is an s orbital]. Using the fixed-core HF representation for the Ψ_n wave function yields

$$\Psi_n(\mathbf{r}_1\sigma_1,\mathbf{r}_2\sigma_2)=\frac{1}{\sqrt{2(1\pm|S_{1s,n}|^2)}}\times\{\varphi_{1s}(\mathbf{r}_1)\varphi_n(\mathbf{r}_2)\pm\varphi_{1s}(\mathbf{r}_2)\varphi_n(\mathbf{r}_1)\}\times S_{S^nM_S^n}(\sigma_1\sigma_2) \tag{30}$$

with $S^n=0$ or 1. If $S^n=0$, then $L^n\neq 0$ in the case under consideration. Under these conditions,

$$\int d\mathbf{r}\,\varphi_n^*(\mathbf{r})\varphi_m(\mathbf{r})=0 \tag{31}$$

for $m\neq n$, due either to orthogonality of the angular parts or, in the case of $S^n=1$ and $L^n=0$, to the fact that φ_n and φ_m are solutions of the same one-electron eigenvalue equation. For the transition density matrix, one then obtains

$$X_n^m(\mathbf{r}\sigma,\mathbf{r}'\sigma')=\frac{1}{\sqrt{1\pm|S_{1s,n}|^2}\sqrt{1+|S_{1s,n}|^2}}\times\int d\mathbf{r}_2\{\varphi_{1s}^*(\mathbf{r})\varphi_n^*(\mathbf{r}_2)\pm\varphi_{1s}^*(\mathbf{r}_2)\varphi_n^*(\mathbf{r})\}\{\varphi_{1s}(\mathbf{r}')\varphi_m(\mathbf{r}_2)-\varphi_{1s}(\mathbf{r}_2)\varphi_m(\mathbf{r}')\}\times\int d\sigma_2 S^*_{S^nM_S^n}(\sigma,\sigma_2)S_{S^mM_S^m}(\sigma',\sigma_2)\equiv X_n^m(\mathbf{r}\mathbf{r}')S^{S^mM_S^m}_{S^nM_S^n}(\sigma,\sigma')\ , \tag{32}$$

where the first factor on the right-hand side of Eq. (32) contains the spatial dependence and the second factor the spin dependence. From the definitions in Eq. (32),

$$X_n^m(\mathbf{r},\mathbf{r}')=\frac{1}{\sqrt{(1\pm|S_{1s,n}|^2)(1-|S_{1s,m}|^2)}}\times[\varphi_n^*(\mathbf{r})\varphi_m(\mathbf{r}')\pm\varphi_n^*(\mathbf{r})\varphi_{1s}(\mathbf{r})S_{1s,m}-\varphi_{1s}^*(\mathbf{r})\varphi_m(\mathbf{r}')S_{n,1s}]\ , \tag{33}$$

where

$$S_{1s,m}=\int d\mathbf{r}\,\varphi_{1s}^*(\mathbf{r})\varphi_m(\mathbf{r})\ , \tag{34a}$$

$$S_{n,1s}=\int d\mathbf{r}\,\varphi_n^*(\mathbf{r})\varphi_{1s}(\mathbf{r})\ , \tag{34b}$$

and Eq. (31) was used. If n refers to a non-S state, then $S_{n,1s}=0$ due to orthogonality of the angular parts of the orbitals and

$$X_n^m(\mathbf{r}\mathbf{r}')=\varphi_n^*(\mathbf{r})\bar{\varphi}_m(\mathbf{r}')\ , \tag{35}$$

where

$$\bar{\varphi}_m(\mathbf{r}')=\frac{1}{\sqrt{(1+|S_{1s,m}|^2)}}[\varphi_m(\mathbf{r}')-\varphi_{1s}(\mathbf{r}')S_{1s,m}]\ . \tag{36}$$

Similarly, if n refers to a ^3S state, it is a good approximation to assume that $S_{1s,m}\simeq 0$, which yields

$$X_n^m(\mathbf{r}\mathbf{r}')\cong\bar{\varphi}_m^*(\mathbf{r})\bar{\varphi}_m(\mathbf{r}')\ , \tag{37}$$

where

$$\bar{\varphi}_n(\mathbf{r})=\frac{1}{\sqrt{1\pm|S_{1s,n}|^2}}[\varphi_n(\mathbf{r})-S_{n,1s}\varphi_{1s}(\mathbf{r})] \tag{38}$$

and the products of the overlap integrals $S_{n,1s}S_{1s,m}$ was assumed to be negligible. In either case, a space-spin factorized form for $X_n^m(\mathbf{r}\mathbf{r}')$ is again obtained.

2. *Excited-state to excited-state transition density matrix when a ^1S state is involved*

When either n or m, or both, refers to a ^1S excited state of helium, the Cohen-McEachran representation of the wave function

$$\Psi_n(\mathbf{r}_1\sigma_1,\mathbf{r}_2\sigma_2)=N_n[\varphi_0(\mathbf{r}_1)\varphi_n(\mathbf{r}_2)\pm\varphi_0(\mathbf{r}_2)\varphi_n(\mathbf{r}_1)]\times S_{S^nM_S^n}(\sigma_1\sigma_2)\quad(S^n=0\ \text{or}\ 1) \tag{39}$$

was employed and an analogous form for Ψ_m was assumed. The transition density matrix then becomes

$$\begin{aligned}X_n^m(\mathbf{r}\sigma,\mathbf{r}'\sigma')&=N_nN_m\int d\mathbf{r}_2[\varphi_0^*(\mathbf{r})\varphi_n^*(\mathbf{r}_2)\pm\varphi_0^*(\mathbf{r}_2)\varphi_n^*(\mathbf{r})][\varphi_0(\mathbf{r}')\varphi_m(\mathbf{r}_2)\pm\varphi_0(\mathbf{r}_2)\varphi_m(\mathbf{r}')]\\&\quad\times\int d\sigma_2 S_{S^nM_S^n}(\sigma_1\sigma_2)S_{S^mM_S^m}(\sigma'\sigma_2)\\&=N_nN_m\Big[\int d\mathbf{r}_2\varphi_n^*(\mathbf{r}_2)\varphi_m(\mathbf{r}_2)\varphi_0^*(\mathbf{r})\varphi_0(\mathbf{r}')\pm\int d\mathbf{r}_2\varphi_n^*(\mathbf{r}_2)\varphi_0(\mathbf{r}_2)\varphi_0^*(\mathbf{r})\varphi_m(\mathbf{r}')\pm\int d\mathbf{r}_2\varphi_0^*(\mathbf{r}_2)\varphi_m(\mathbf{r}_2)\varphi_n^*(\mathbf{r})\varphi_0(\mathbf{r}')\\&\quad\pm\int d\mathbf{r}_2\varphi_0^*(\mathbf{r}_2)\varphi_0(\mathbf{r}_2)\varphi_n^*(\mathbf{r})\varphi_m(\mathbf{r}')\Big]\int d\sigma_2 S_{S^mM_S^n}(\sigma\sigma_2)S_{S^mM_S^m}(\sigma'\sigma_2)\\&=N_nN_m[S_{n,m}\varphi_0^*(\mathbf{r})\varphi_0(\mathbf{r}')\pm S_{n,0}\varphi_0^*(\mathbf{r})\varphi_m(\mathbf{r}')\pm S_{0,m}\varphi_n^*(\mathbf{r})\varphi_0(\mathbf{r}')\pm\varphi_n^*(\mathbf{r})\varphi_m(\mathbf{r}')]\\&\quad\times\int d\sigma_2 S_{S^nM_S^n}(\sigma\sigma_2)S_{S^mM_S^m}(\sigma'\sigma_2)\ .\end{aligned} \tag{40}$$

If both n and m refer to singlet states (i.e., if $S^n=S^m=0$ and $L^n=0$ or $L^m=0$, or $L^n=L^m=0$), then

$$S_{n,m}=0\ , \tag{41}$$

because the $\varphi_n(\mathbf{r})$ and $\varphi_m(\mathbf{r})$ functions are eigenfunctions of the same eigenvalue problem with different eigenvalues. Equation (40) then simplifies to

$$\begin{aligned}X_n^m(\mathbf{r}\sigma,\mathbf{r}'\sigma')=N_nN_m[&\pm S_{0,m}\varphi_0(\mathbf{r})\varphi_n^*(\mathbf{r})\\&\pm S_{n,0}\varphi_0^*(\mathbf{r})\varphi_m(\mathbf{r}')\\&+\varphi_n^*(\mathbf{r})\varphi_m(\mathbf{r}')]\\&\times[\alpha(\sigma)\alpha^*(\sigma')+\beta(\sigma)\beta^*(\sigma)].\end{aligned} \tag{42}$$

The approximations

$$S_{0,m}\approx 0,\quad S_{n,0}\approx 0 \tag{43}$$

are again made and Eq. (42) becomes

$$X_n^m(\mathbf{r}\sigma,\mathbf{r}'\sigma')\approx\varphi_n^*(\mathbf{r})\varphi_m(\mathbf{r}')[\alpha(\sigma)\alpha^*(\sigma')+\beta(\sigma)\beta^*(\sigma')]\ . \tag{44}$$

Alternatively, if it is assumed that

$$S_{0,m}S_{n,0}\approx 0\ , \tag{45}$$

then Eq. (42) becomes

$$X_n^m(\mathbf{r}\sigma,\mathbf{r}'\sigma')\approx\bar{\varphi}_n^*(\mathbf{r})\bar{\varphi}_m(\mathbf{r}')[\alpha(\sigma)\alpha^*(\sigma')+\beta(\sigma)\beta^*(\sigma')]\ , \tag{46}$$

where

$$\bar{\varphi}_n(\mathbf{r})=\varphi_n(\mathbf{r})+S_{n,0}\varphi_0(\mathbf{r})\ , \tag{47a}$$

$$\bar{\varphi}_m(\mathbf{r})=\varphi_m(\mathbf{r})+S_{0,m}\varphi_0(\mathbf{r})\ . \tag{47b}$$

It should be noted here that if one of the states is triplet and the other is singlet, Eq. (41) does not generally apply. However, the approximations

$$S_{n,m}\approx 0,\quad S_{n,0}\approx 0,\quad S_{0,m}\approx 0 \tag{48}$$

are generally accurate because, in this case only, a relatively small exchange term is present in the scattering matrix. Equation (42) then takes the form

$$\begin{aligned}&X_n^m(\mathbf{r}\sigma,\mathbf{r}'\sigma')\\&\approx\varphi_n^*(\mathbf{r})\varphi_m(\mathbf{r}')\int d\sigma_2 S_{S^nM_S^n}(\sigma\sigma_2)S_{S^mM_S^m}(\sigma'\sigma_2)\ .\end{aligned} \tag{49}$$

3. *Simplification of the transition density matrix*

In the general formulation given in paper I, the excited-state–excited-state transition density matrix [see Eq. (42) in paper I] was written as

$$\begin{aligned}X_n^m(\mathbf{r}\sigma,\mathbf{r}'\sigma')=&\sum_{k,q}(-1)^{k-q}C^{k\,S^mS^n}_{q\,M_S^mM_S^n}\xi_{k,-q}(\sigma\sigma')\\&\times X_n^{m(k)}(\mathbf{r}\mathbf{r}')\ .\end{aligned} \tag{50}$$

Because some of the contributions to the T-matrix elements (specifically T^{V} and T^{VI}) were expressed in terms of the $X_n^{m(k)}(\mathbf{r}\mathbf{r}')$ quantities [see Eq. (44'''') in I], a correspondence needs to be made to Eqs. (22), (35), (37), (44), and (49) in Sec. II B 2. This correspondence is made using the following expression for the spin factor on the right-hand side of Eq. (32):

$$\begin{aligned}S^{S^mM_s^m}_{S^nM_S^n}(\sigma\sigma')=&[(2S^m+1)]^{1/2}(-1)^{1+S^n}\\&\times\sum_{k,q}(2k+1)^{1/2}(-1)^{k-q}\\&\times C^{k\,S^mS^n}_{q\,M_S^mM_S^n}\begin{Bmatrix}S^n & S^m & k\\ \frac{1}{2} & \frac{1}{2} & \frac{1}{2}\end{Bmatrix}\xi_{k,-q}(\sigma\sigma')\ ,\end{aligned} \tag{51}$$

where

$$\begin{Bmatrix}a & b & c\\ d & e & f\end{Bmatrix}$$

refers to the $6j$ symbol [8]. A comparison of Eq. (50) with Eqs. (32) and (51) results in the identification of the relation

$$\begin{aligned}X_n^{m(k)}(\mathbf{r}\mathbf{r}')=&X_n^m(\mathbf{r}\mathbf{r}')[(2S^m+1)]^{1/2}(-1)^{1+S^n}\\&\times(2k+1)^{1/2}\begin{Bmatrix}S^n & S^m & k\\ \frac{1}{2} & \frac{1}{2} & \frac{1}{2}\end{Bmatrix}\ .\end{aligned} \tag{52}$$

In the two special cases of interest here, namely, $S^m=1$ and $S^n=0$, and $S^m=1$ and $S^n=1$, Eq. (52) reduces to (respectively)

$$\left.\begin{aligned}&X_n^{m(1)}(\mathbf{r}\mathbf{r}')=-\left[\frac{3}{2}\right]^{1/2}X_n^m(\mathbf{r}\mathbf{r}')\\&X_n^{m(k)}(\mathbf{r}\mathbf{r}')=0\quad\text{for } k\neq 1\end{aligned}\right\}(S^m=1,\ S^n=0)\ , \tag{53}$$

$$\left.\begin{aligned}&X_n^{m(0)}(\mathbf{r}\mathbf{r}')=\frac{1}{\sqrt{2}}X_n^m(\mathbf{r}\mathbf{r}')\\&X_n^{m(1)}(\mathbf{r}\mathbf{r}')=-X_n^m(\mathbf{r}\mathbf{r}')\\&X_n^{m(k)}(\mathbf{r}\mathbf{r}')=0\quad\text{for } k\neq 0,1\end{aligned}\right\}(S^m=1,\ S^n=1)\ . \tag{54}$$

4. *Formulation of the T matrix*

Substitution of $X_m(\mathbf{r}\sigma,\mathbf{r}'\sigma')$ [as given by Eq. (10)] into Eqs. (33) and (38) in paper I [or the substitution of $X_m(rr')$ as given by Eq. (13) into Eqs. (55) and (56) in I] is straightforward and not detailed here. However, the following additional detail on the form of the resulting T matrix is useful for computations. Using the approximations for $X_m(\mathbf{r}\mathbf{r}')$, $\tilde{X}_n(\mathbf{r}\mathbf{r}')$, and $X_n^m(\mathbf{r}\mathbf{r}')$ in Eqs. (43)–(43'''') and (44)–(44'''') of paper I (the superscript notation for the orbitals are implied, but suppressed here for simplicity) one obtains

$$I_s=(-1)^{S^n}\tilde{I}_s\quad(s=1,2,\ldots,5)\ , \tag{55a}$$

$$I_6^{(k)}=(-1)^{S^n}\tilde{I}_6^{(k)}\quad(k=0,1,\ldots)\ , \tag{55b}$$

where

$$\tilde{I}_1=\int d\mathbf{r}\,d\mathbf{r}' f_{\mathbf{q}}^{m(-)*}(\mathbf{r}) f_{\mathbf{p}}^{(+)}(\mathbf{r}) V(\mathbf{r}-\mathbf{r}') \varphi_{1s}(\mathbf{r}') \varphi_n^*(\mathbf{r}') , \tag{56a}$$

$$\tilde{I}_2=\int d\mathbf{r}\,d\mathbf{r}' f_{\mathbf{q}}^{(-)*}(\mathbf{r}) \tilde{f}_{\mathbf{p}}^{m(+)}(\mathbf{r}) V(\mathbf{r}-\mathbf{r}') \varphi_{1s}(\mathbf{r}') \varphi_n^*(\mathbf{r}') , \tag{56b}$$

$$\tilde{I}_3=\int d\mathbf{r}\,d\mathbf{r}' f_{\mathbf{q}}^{m(-)*}(\mathbf{r}') f_{\mathbf{p}}^{(+)}(\mathbf{r}) V(\mathbf{r}-\mathbf{r}') \varphi_{1s}^*(\mathbf{r}) \varphi_n(\mathbf{r}') , \tag{56c}$$

$$\tilde{I}_4=\int d\mathbf{r}\,d\mathbf{r}' f_{\mathbf{q}}^{m(-)*}(\mathbf{r}') f_{\mathbf{p}}^{(+)}(\mathbf{r}) V(\mathbf{r}-\mathbf{r}') \varphi_{1s}^*(\mathbf{r}) \varphi_n(\mathbf{r}') , \tag{56d}$$

$$\tilde{I}_5=\delta_{S^n S^m}\frac{1}{\sqrt{2}}\int d\mathbf{r}\,d\mathbf{r}' f_{\mathbf{q}}^{(-)*}(\mathbf{r}) f_{\mathbf{p}}^{(+)}(\mathbf{r}) V(\mathbf{r}-\mathbf{r}') \varphi_n^*(\mathbf{r}') \varphi_m(\mathbf{r}') , \tag{56e}$$

$$\tilde{I}_6^{(k)}=-[(2S^m+1)]^{1/2}(2k+1)^{1/2}\begin{Bmatrix} S^n & S^m & k \\ \frac{1}{2} & \frac{1}{2} & \frac{1}{2} \end{Bmatrix}\int d\mathbf{r}\,d\mathbf{r}' f_{\mathbf{q}}^{(-)*}(\mathbf{r}) f_{\mathbf{p}}^{(+)}(\mathbf{r}') V(\mathbf{r}-\mathbf{r}') \varphi_n^*(\mathbf{r}) \varphi_m(\mathbf{r}')$$

$$\equiv -[(2S^m+1)]^{1/2}(2k+1)^{1/2}\begin{Bmatrix} S^n & S^m & k \\ \frac{1}{2} & \frac{1}{2} & \frac{1}{2} \end{Bmatrix}\tilde{I}_6 . \tag{56f}$$

Partial-wave expansions for the functions appearing in Eqs. (56a)-(56f) are introduced as follows [Eqs. (45), (51), and (52) in paper I]. Introducing the unit-amplitude normalized radial functions by $p_{p,l}(r), p_{q,l}(r)$, by the definitions

$$p_{p,l}(r)=\left[\frac{\pi p}{2}\right]^{1/2} P_{p,l}(r) , \tag{57a}$$

$$p_{q,l}(r)=\left[\frac{\pi q}{2}\right]^{1/2} P_{q,l}(r) , \tag{57b}$$

with the asymptotic behavior of

$$p_{p,l}(r) \underset{r\to\infty}{\to} \sin\left[pr-\frac{l\pi}{2}+\delta_l(p)\right] , \tag{58a}$$

$$p_{q,l}(r) \underset{r\to\infty}{\to} \sin\left[qr-\frac{l\pi}{2}+\delta_l(q)\right] , \tag{58b}$$

the $f_{p,l}(r)$ and $g_{q,l}(r)$ functions in paper I can be defined by

$$f_{p,l}(r)=\left[\frac{\pi p}{2}\right]^{1/2} F_{p,l}(r) , \tag{59a}$$

$$g_{q,l}(r)=\left[\frac{\pi q}{2}\right]^{1/2} G_{q,l}(r) . \tag{59b}$$

The resulting integro-differential equations for $f_{p,l}$ and $g_{q,l}$ functions are then obtained from Eqs. (55) and (56) of paper I by simply replacing $F_{p,l}$ by $f_{q,l}$, $G_{q,l}$ by $g_{q,l}$, and $P_{p,l}$ and $P_{q,l}$ by $p_{p,l}$ and $p_{q,l}$, respectively.

The $P_{1s}(r)$, $P_n(r)$, and $P_m(r)$ orbitals are introduced by the definition

$$P_i(r)=rR_i(r) \quad (i=1s,n,m) . \tag{60}$$

Choosing the z axis along the momentum $\mathbf{p}$ of the incident electron and denoting the polar angle of the $\mathbf{q}$ vector by θ (the momentum of the scattered electron), the polar coordinates of $\mathbf{q}$ became $(q,\theta,0)$. To simplify the notation, L^n will be written as L, M_L^n as M_L, and $L^m=M_L^m=0$ was assumed at the outset because the metastable states are S states.

Finally introducing the notation,

$$\Delta(l_p,l_q)=\delta_{l_p}(p)+\delta_{l_q}(q) , \tag{61}$$

$$[l]=2l+1 , \tag{62}$$

with $P_l^m(x)$ as the associated Legendre function [8], the partial-wave expansions of the integrals $\tilde{I}_s$ $(s=1,2,\ldots,6)$ become

$$\tilde{I}_1=\frac{4\pi}{pq}\sum_{l_p,l_q} i^{l_p-l_q}e^{i\Delta(l_p,l_q)}\left[\frac{[l_q]}{[L]}\right]^{1/2} C^{l_q}_{-M_L\ L\ M_L}\,C^{l_q}_{0\ 0\ 0}\,C^{L\ l_p}_{0\ 0}\left[\frac{(l_q-M_L)!}{(l_q+M_L)!}\right]^{1/2}$$

$$\times\int\int dr\,dr' p_{p,l_p}(r) g_{q,l_q}(r)\frac{r_<^L}{r_>^{L+1}} P_n(r') P_{1s}(r') P_{l_q}^{M_L}(\cos\theta) , \tag{63}$$

$$\tilde{I}_2=\frac{4\pi}{pq}\sum_{l_p,l_q} i^{l_p-l_q}e^{i\Delta(l_p,l_q)}\left[\frac{[l_q]^2}{[L][l_p]}\right]^{1/2} C^{l_q}_{-M_L\ L\ M_L}\,C^{l_q}_{0\ 0\ 0}\,C^{L\ l_p}_{0\ 0}\left[\frac{(l_q-M_L)!}{(l_q+M_L)!}\right]^{1/2}$$

$$\times\int dr\,dr' p_{q,l_q}(r) f_{p,l_p}^m(r)\frac{r_<^L}{r_>^{L+1}} P_n(r') P_{1s}(r') P_{l_q}^{M_L}(\cos\theta) , \tag{64}$$

$$\tilde{I}_3=\frac{4\pi}{pq}\sum_{l_p,l_q} i^{l_p-l_q}e^{i\Delta(l_p,l_q)}\left[\frac{[L]}{[l_q]}\right]^{1/2} C^{l_q}_{-M_L\ M_L\ 0}\,C^{l_q\ L\ l_p}_{0\ 0\ 0}\left[\frac{(l_q-M_L)!}{(l_q+M_L)!}\right]^{1/2}$$
$$\times\int dr\,dr' g_{q,l_q}(r')p_{p,l_p}(r)\frac{r_<^{l_q}}{r_>^{l_q+1}}P_n(r')P_{1s}(r')P_{l_q}^{M_L}(\cos\theta)\ , \tag{65}$$

$$\tilde{I}_4=\frac{4\pi}{pq}\sum_{l_p,l_q} i^{l_p-l_q}e^{i\Delta(l_p,l_q)}\left[\frac{[L]}{[l_q]}\right]^{1/2} C^{l_q}_{-M_L\ M_L\ 0}\,C^{l_q\ L\ l_p}_{0\ 0\ 0}\left[\frac{(l_q-M_L)!}{(l_q+M_L)!}\right]^{1/2}$$
$$\times\int dr\,dr' p_{q,l_q}(r')f_{p,l_p}(r)\frac{r_<^{l_q}}{r_>^{l_q+1}}P_n(r')P_{1s}(r')P_{l_q}^{M_L}(\cos\theta)\ , \tag{66}$$

$$\tilde{I}_5=\delta_{S^nS^m}\frac{4\pi}{pq}\sum_{l_p,l_q} i^{l_p-l_q}e^{i\Delta(l_p,l_q)}\left[\frac{[l_q]^2}{[L]}\right]^{1/2} C^{l_q}_{-M_L\ M_L\ 0}\,C^{l_q\ L\ l_p}_{0\ 0\ 0}\left[\frac{(l_q-M_L)!}{(l_q+M_L)!}\right]^{1/2}$$
$$\times\int dr\,dr' p_{p,l_p}(r)p_{q,l_q}(r)\frac{r_<^{L}}{r_>^{L+1}}P_n(r')P_m(r')P_{l_q}^{M_L}(\cos\theta)\ , \tag{67}$$

$$\tilde{I}_6=\frac{4\pi}{pq}\sum_{l_p,l_q} i^{l_p-l_q}e^{i\Delta(l_p,l_q)}([L])^{1/2}C^{l_q}_{-M_L\ M_L\ 0}\,C^{l_q\ L\ l_p}_{0\ 0\ 0}\left[\frac{(l_q-M_L)!}{(l_q+M_L)!}\right]^{1/2}$$
$$\times\int dr\,dr' p_{p,l_p}(r)p_{q,l_q}(r')\frac{r_<^{l_q}}{r_>^{l_q+1}}P_n(r)P_m(r')P_{l_q}^{M_L}(\cos\theta)\ . \tag{68}$$

The numerical results reported here were obtained using the above expressions for $\tilde{I}_s$ $(s=1,2,\ldots,5)$ and $\tilde{I}_6^k$ $(k=0,1)$ and the cross-section formulas given by Eqs. (58b) and (58d) of paper I.

In our DWA calculations the same formulas were used for the T matrices, but the $f_{\mathbf{p}}^{(+)}(\mathbf{r})$ and $f_{\mathbf{q}}^{(-)}(\mathbf{r})$ distorted-wave orbitals were calculated in the static-exchange potentials of the initial and final states, respectively. In the case of degenerate target states (e.g., ^3S or ^3P) an average field (in M_L and M_S) was used.

III. RESULTS AND DISCUSSION

FOMBT differs from the usual distorted-wave approximation for excitation from excited electronic states in that the free-electron wave functions are "distorted" by the ground state of the target and channel coupling to the "elastic channel" is incorporated into the T matrix. In order to obtain information about the magnitude of the various terms in the FOMBT model for the cross sections, calculations were performed in which channel-coupling effects were neglected [$I_S=0$ $(s=1,2,3,4)$]. This approximation, denoted by FOMBT(1), is basically the same as the usual distorted-wave approximation, except here the distorted-wave orbitals are calculated in the static-exchange field of the *ground* state [the reference state for the MBT formulation of the scattering problem]. A second approximation, denoted by FOMBT(2) in the tables, which uses all terms for final energies $\varepsilon_q>\omega_n$ but

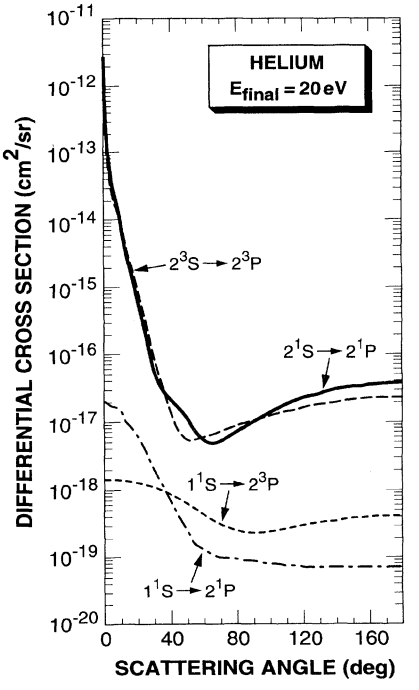

FIG. 2. Differential cross sections (DCSs) for excitation of the $2\,^1P$ and $2\,^3P$ states from the $2\,^1S$ and $2\,^3S$ metastable states, respectively, of helium for 20-eV scattered (i.e., final) electron energy using FOMBT(1). DCSs for excitation of the same final states from the helium ground state ($1\,^1S$), for the same final electron energy, are also shown to illustrate the large size and strong forward peaking of the DCSs for excitation from the metastable states.

assumes $I_1 = I_2 = 0$ when $\varepsilon_q < \omega_n$, was also evaluated (for a few cases) specifically to determine the effect of channel coupling.

A. Differential cross sections

The differential and integral cross sections for excitation from the metastable states in helium are very large relative to excitation to the same final state from the ground state. To illustrate the size of these excitation cross sections, Fig. 2 compares the calculated differential cross sections (DCSs) for excitation to the $2\,^1P$ and $2\,^3P$ states from the two metastable helium states with that from the ground state. Two points are worth making about the comparison in Fig. 2. The first is that the DCSs for excitation from the two metastable S states range from a factor of 10^1 to 10^5 times larger than those from the ground state, depending on the scattering angle. The second is that the shapes of the DCSs for $2\,^{1,3}S \rightarrow 2\,^{1,3}P$ excitation are very similar, perhaps not surprisingly. Comparisons with the available experimen-

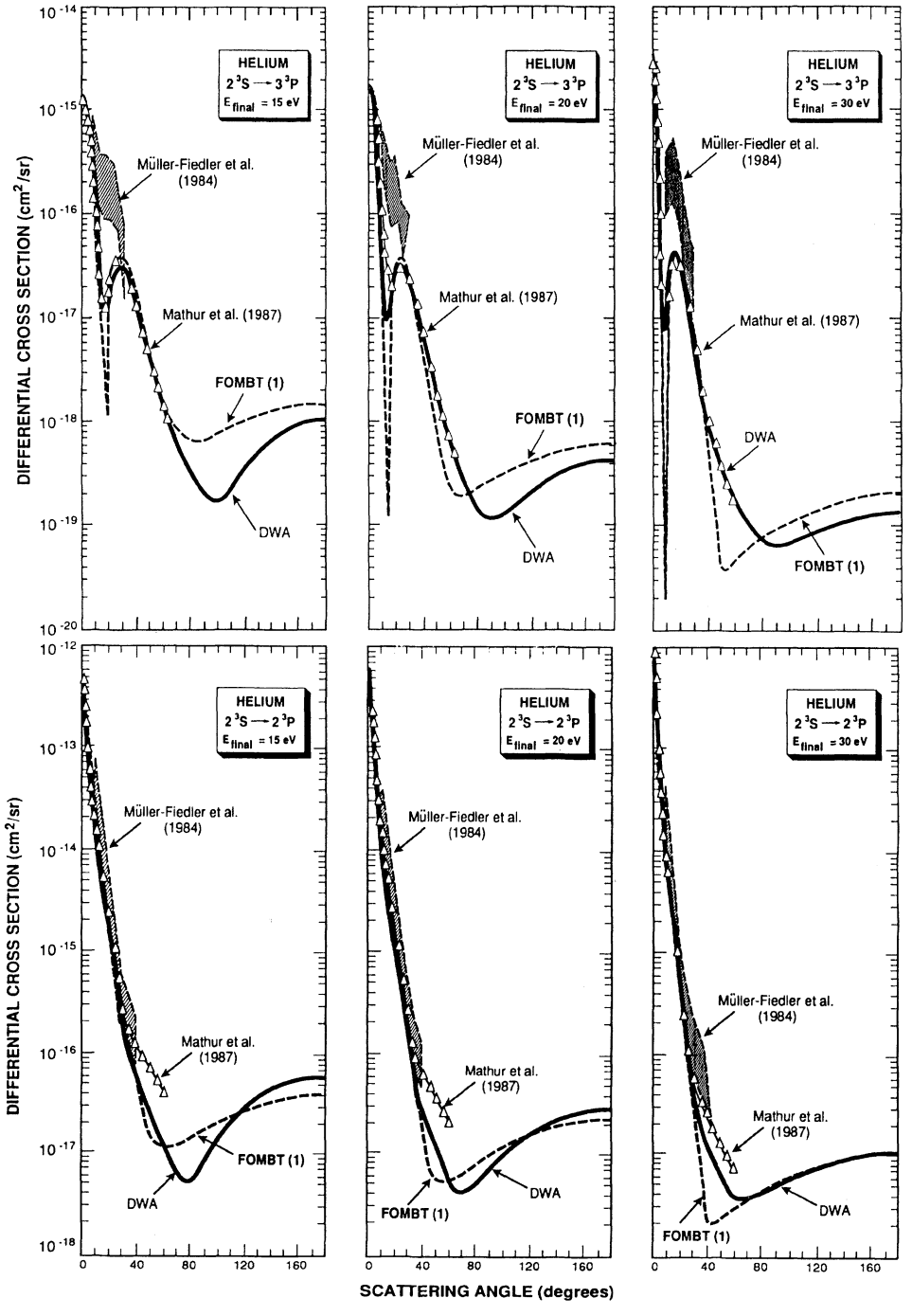

FIG. 3. Comparison of DWA results of Mathur *et al.* [10] and present FOMBT(1) DCS results with the experimental results of Müller-Fiedler *et al.* [9] for electron-impact excitation from the $2\,^3S$ metastable state to the $2\,^3P$ (lower half of the figure) and $3\,^3P$ (upper half) states in helium. In both the upper and lower halves of the figure, the three panels are (a) 15-eV final electron energy (left panel), (b) 20-eV final electron energy (middle panel), and (c) 30-eV final electron energy (right panel).

tal and theoretical results on the DCSs are made in the following sections.

1. $2\,^3S \rightarrow 2\,^3P, 3\,^3P$

Figure 3 compares DWA and FOMBT(1) DCS results obtained from this study with the experimental results from Müller-Fiedler *et al.* [9] and the DWA results from Mathur *et al.* [10], for excitation of the $2\,^3P$ and $3\,^3P$ states of helium. The experimental data were obtained at selected values for the energy of the scattered electron as indicated in the upper right-hand corner of each panel in Fig. 3. The agreement between the theoretical models and experiment is generally very good over the limited angular range covered by the experiment for the $2\,^3S \rightarrow 2\,^3P$ excitation, but not quite as good for the $2\,^3S \rightarrow 3\,^3P$ excitation. However, at scattering angles just beyond the range of the experimental data, the theoretical results begin to differ in the shapes they predict for the DCSs. The difference between the results from FOMBT(1) and DWA can be attributed directly to differences in the treatment of distortion of the continuum electron in these two models. That is, our DWA calculation incorporates distortion of the incident and scattered electrons by the static exchange field of the initial

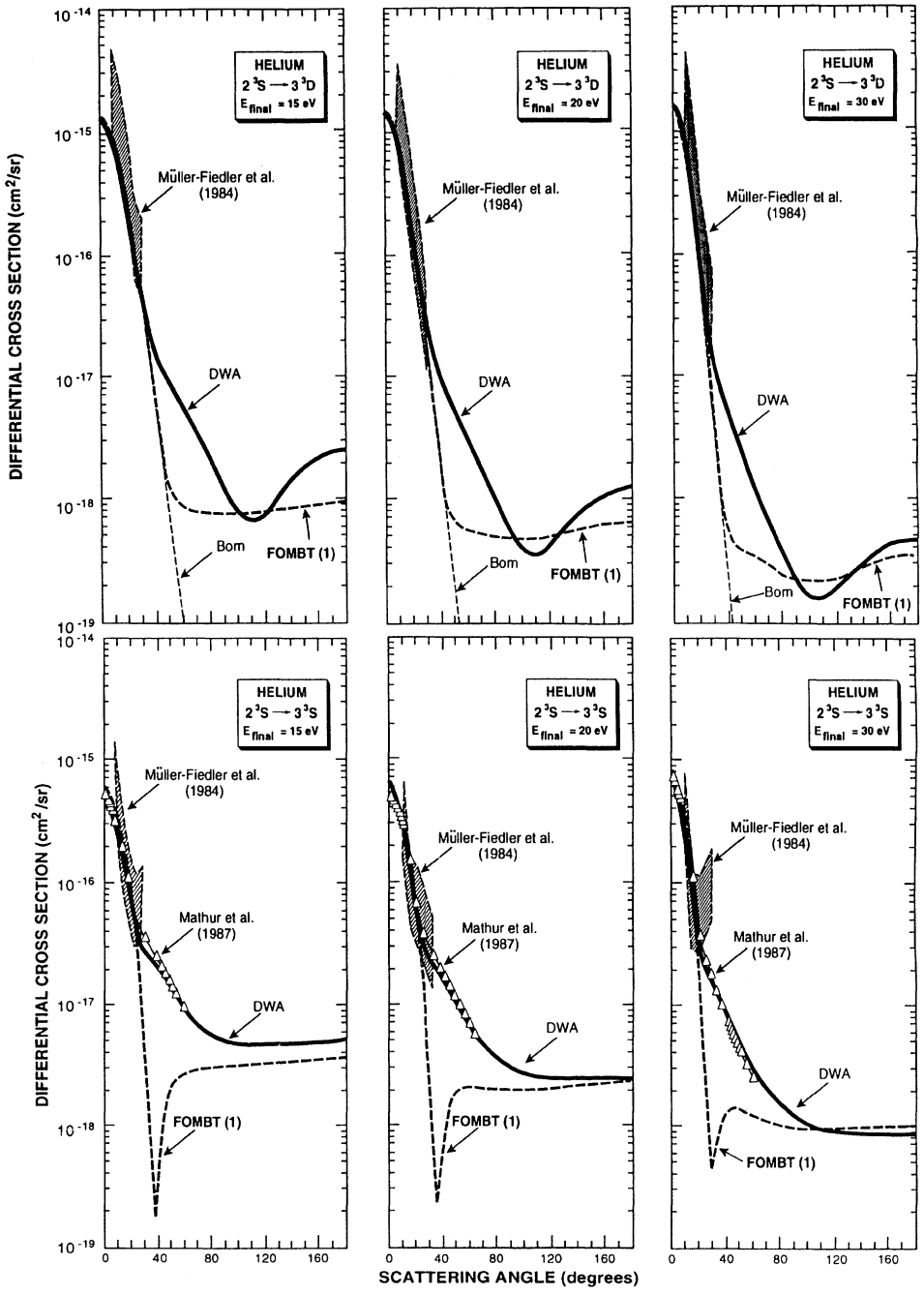

FIG. 4. Comparison of present FOMBT(1) DCSs with the experimental results of Müller-Fiedler *et al.* [9] for the $2\,^3S \rightarrow 3\,^3S$ (lower) and $3\,^3D$ (upper) electron-impact-induced transitions for (a) 15-eV final electron energy (left panel), (b) 20-eV final electron energy (middle panel), and (c) 30-eV final electron energy (right panel). The DWA curves denote the DWA results from Mathur *et al.* [10]. The notation is the same as in Fig. 3.

(metastable) and final excited state, respectively, while FOMBT(1) is required by MBT to incorporate distortion on both electrons by the ground state of the target. That is, distortion effects by the actual initial and final target states first appear in second-order MBT. The results from Mathur *et al.* [10] were obtained using the same distortion potentials as used in our DWA model and also incorporate a correction to account for polarization of the target by the incident and scattered electrons. It is important (and somewhat surprising) to note that, based on the comparisons in Fig. 3, target polarization appears to be a small physical effect for helium excitation at incident electron energies greater than about 16 eV. This result is somewhat surprising because polarization of the diffuse electron cloud of these metastable initial states by the incident electron is generally believed to have a strong effect on the DCS, particularly at the smaller scattering angles for low and medium energies. At

TABLE I. DCSs (cm^2/sr) for electron-impact excitation $2\,^3S \rightarrow 2\,^3P$ for scattered electron energies of 15, 20, and 30 eV. The present DWA and FOMBT(1) results are described in the text. The results from Mathur *et al.* are from Ref. [10]. The numbers in brackets denote multiplicative powers of 10.

Angle / E (final)	15 eV			20 eV			30 eV		
(deg)	DWA	FOMBT(1)	Mathur *et al.*	DWA	FOMBT(1)	Mathur *et al.*	DWA	FOMBT(1)	Mathur *et al.*
0	4.43[−13]	4.51[−13]	4.64[−13]	5.97[−13]	6.05[−13]	6.18[−13]	9.04[−13]	9.12[−13]	9.24[−13]
1	3.60[−13]	3.67[−13]	3.79[−13]	4.27[−13]	4.33[−13]	4.46[−13]	4.81[−13]	4.86[−13]	5.00[−13]
2	2.30[−13]	2.35[−13]	2.44[−13]	2.29[−13]	2.32[−13]	2.41[−13]	1.98[−13]	2.00[−13]	2.07[−13]
3			1.51[−13]			1.34[−13]			1.02[−13]
4	9.19[−14]	9.40[−14]	9.68[−14]	7.72[−14]	7.87[−14]	8.09[−14]	5.59[−14]	5.67[−14]	5.79[−14]
5			6.52[−14]			5.23[−14]			3.60[−14]
6	4.39[−14]	4.52[−14]	4.56[−14]	3.46[−14]	3.54[−14]	3.56[−14]	2.33[−14]	2.38[−14]	2.38[−14]
7			3.29[−14]			2.52[−14]			1.64[−14]
8	2.40[−14]	2.49[−14]	2.44[−14]	1.82[−14]	1.88[−14]	1.83[−14]	1.16[−14]	1.19[−14]	1.15[−14]
9			1.84[−14]			1.36[−14]			8.35[−15]
10	1.43[−14]	1.49[−14]	1.42[−14]	1.04[−14]	1.08[−14]	1.03[−14]	6.22[−15]	6.49[−15]	6.11[−15]
15			4.33[−15]			2.87[−15]			1.44[−15]
20	1.66[−15]	1.90[−15]	1.50[−15]	9.70[−16]	1.11[−15]	8.97[−16]	3.88[−16]	4.44[−16]	3.79[−16]
25	6.18[−16]	7.43[−16]	5.77[−16]	3.16[−16]	3.77[−16]	3.19[−16]	1.03[−16]	1.15[−16]	1.22[−16]
30	2.40[−16]	2.94[−16]	2.64[−16]	1.12[−16]	1.27[−16]	1.45[−16]	3.35[−17]	2.82[−17]	5.75[−17]
35	1.06[−16]	1.19[−16]	1.53[−16]	4.82[−17]	4.27[−17]	8.74[−17]	1.62[−17]	6.73[−18]	3.62[−17]
40	5.69[−17]	5.07[−17]	1.08[−16]	2.72[−17]	1.55[−17]	6.20[−17]	1.03[−17]	2.28[−18]	2.52[−17]
45	3.67[−17]	2.47[−17]	8.33[−17]	1.80[−17]	7.36[−18]	4.62[−17]	7.10[−18]	1.86[−18]	1.77[−17]
50	2.58[−17]	1.51[−17]	6.55[−17]	1.25[−17]	5.34[−18]	3.46[−17]	5.13[−18]	2.23[−18]	1.26[−17]
55	1.82[−17]	1.18[−17]	5.13[−17]	8.76[−18]	5.23[−18]	2.60[−17]	4.00[−18]	2.65[−18]	9.15[−18]
60	1.27[−17]	1.09[−17]	4.02[−17]	6.36[−18]	5.70[−18]	1.97[−17]	3.48[−18]	3.02[−18]	7.06[−18]
65	8.81[−18]	1.12[−17]		5.07[−18]	6.33[−18]		3.37[−18]	3.34[−18]	
70	6.49[−18]	1.18[−17]		4.65[−18]	7.01[−18]		3.48[−18]	3.64[−18]	
75	5.57[−18]	1.28[−17]		4.88[−18]	7.73[−18]		3.73[−18]	3.93[−18]	
80	5.83[−18]	1.38[−17]		5.56[−18]	8.48[−18]		4.60[−18]	4.24[−18]	
85	7.07[−18]	1.50[−17]		6.59[−18]	9.28[−18]		4.40[−18]	4.56[−18]	
90	9.10[−18]	1.63[−17]		7.88[−18]	1.01[−17]		4.76[−18]	4.90[−18]	
95	1.18[−17]	1.77[−17]		9.36[−18]	1.10[−17]		5.15[−18]	5.25[−18]	
100	1.50[−17]	1.91[−17]		1.10[−17]	1.19[−17]		5.56[−18]	5.63[−18]	
105	1.85[−17]	2.06[−17]		1.27[−17]	1.28[−17]		5.96[−18]	6.01[−18]	
110	2.24[−17]	2.22[−17]		1.44[−17]	1.38[−17]		6.37[−18]	6.41[−18]	
115	2.64[−17]	2.37[−17]		1.61[−17]	1.48[−17]		6.79[−18]	6.81[−18]	
120	3.05[−17]	2.53[−17]		1.79[−17]	1.58[−17]		7.21[−18]	7.22[−18]	
125	3.46[−17]	2.68[−17]		1.96[−17]	1.67[−17]		7.62[−18]	7.62[−18]	
130	3.86[−17]	2.83[−17]		2.12[−17]	1.77[−17]		8.02[−18]	8.01[−18]	
135	4.24[−17]	2.97[−17]		2.27[−17]	1.86[−17]		8.38[−18]	8.38[−18]	
140	4.60[−17]	3.10[−17]		2.41[−17]	1.94[−17]		8.71[−18]	8.73[−18]	
145	4.93[−17]	3.23[−17]		2.54[−17]	2.02[−17]		9.02[−18]	9.06[−18]	
150	5.23[−17]	3.34[−17]		2.66[−17]	2.09[−17]		9.32[−18]	9.35[−18]	
155	5.49[−17]	3.43[−17]		2.76[−17]	2.15[−17]		9.57[−18]	9.61[−18]	
160	5.71[−17]	3.52[−17]		2.85[−17]	2.20[−17]		9.76[−18]	9.83[−18]	
165	5.88[−17]	3.58[−17]		2.93[−17]	2.25[−17]		9.90[−18]	1.00[−17]	
170	5.99[−17]	3.63[−17]		2.98[−17]	2.28[−17]		1.00[−17]	1.01[−17]	
175	6.06[−17]	3.66[−17]		3.01[−17]	2.29[−17]		1.01[−17]	1.02[−17]	
180	6.08[−17]	3.67[−17]		3.02[−17]	2.30[−17]		1.02[−17]	1.02[−17]	

scattering angles greater than 40°, the difference between the present DWA results and the DWA results of Mathur *et al.* suggests that polarization may contribute at larger angles.

For the case of the $2\,^3S \rightarrow 3\,^3P$ transition, the agreement between theory and experiment is qualitative, but not quantitative. That is, the experimental results are larger than those from the theory, but they do seem to show the dip predicted by all models at about 20° scattering angle. Note that the magnitude of this DCS is a factor of 100 smaller than that for the $2\,^3P$, which accounts for the larger experimental uncertainty and smaller angular range for the measured DCSs. Based on the excellent agreement between our DWA results and the DWA re-

TABLE II. DCSs (cm^2/sr) for electron-impact excitation $2\,^3S \rightarrow 3\,^3S$ for scattered electron energies of 15, 20, and 30 eV. The present DWA and FOMBT (1) results are described in the text. The results from Mathur *et al.* are from Ref. [10]. The numbers in brackets denote multiplicative powers of 10.

Angle (deg) \ E(final)	15 eV			20 eV			30 eV		
	DWA	FOMBT(1)	Mathur *et al.*	DWA	FOMBT(1)	Mathur *et al.*	DWA	FOMBT(1)	Mathur *et al.*
0	5.14[−16]	6.40[−16]	5.18[−16]	5.64[−16]	6.88[−16]	5.65[−16]	6.32[−16]	7.46[−16]	6.29[−16]
1	5.11[−16]	6.37[−16]	5.16[−16]	5.60[−16]	6.84[−16]	5.61[−16]	6.25[−16]	7.39[−16]	6.23[−16]
2	5.03[−16]	6.28[−16]	5.08[−16]	5.49[−16]	6.71[−16]	5.51[−16]	6.08[−16]	7.19[−16]	6.06[−16]
			4.95[−16]			5.34[−16]			5.80[−16]
4	4.73[−16]	5.92[−16]	4.78[−16]	5.08[−16]	6.23[−16]	5.10[−16]	5.44[−16]	6.46[−16]	5.44[−16]
			4.58[−16]			4.82[−16]			5.02[−16]
6	4.28[−16]	5.38[−16]	4.33[−16]	4.47[−16]	5.51[16]	4.50[−16]	4.53[−16]	5.43[−16]	4.55[−16]
			4.06[−16]			4.15[−16]			4.06[−16]
8	3.72[−16]	4.72[−16]	3.77[−16]	3.75[−16]	4.66[−16]	3.78[−16]	3.53[−16]	4.27[−16]	3.56[−16]
			3.48[−16]			3.41[−16]			3.08[−16]
10	3.12[−16]	3.98[−16]	3.18[−16]	2.30[−16]	3.75[−16]	3.04[−16]	2.58[−16]	3.14[−16]	2.62[−16]
12	2.53[−16]	3.24[−16]		2.30[−16]	2.89[−16]		1.79[−16]	2.17[−16]	
14	1.98[−16]	2.54[−16]		1.69[−16]	2.12[−16]		1.18[−16]	1.41[−16]	
15			1.80[−16]			1.50[−16]			1.01[−16]
16	1.51[−16]	1.93[−16]		1.21[−16]	1.49[−16]		7.64[−17]	8.56[−17]	
20	8.45[−17]	9.90[−17]	9.24[−17]	6.10[−17]	6.40[−17]	6.83[−17]	3.45[−17]	2.59[−17]	3.98[−17]
25	4.37[−17]	3.43[−17]	5.16[−17]	3.14[−17]	1.63[−17]	3.72[−17]	2.02[−17]	3.54[−18]	2.28[−17]
30	2.98[−17]	8.43[−18]	3.55[−17]	2.33[−17]	2.39[−18]	2.65[−17]	1.61[−17]	4.37[−19]	1.65[−17]
35	2.52[−17]	9.87[−19]	2.83[−17]	2.00[−17]	2.29[−19]	2.09[−17]	1.28[−17]	8.41[−19]	1.21[−17]
40	2.22[−17]	1.78[−19]	2.31[−17]	1.68[−17]	8.06[−19]	1.64[−17]	9.61[−18]	1.27[−18]	8.54[−18]
45	1.88[−17]	9.93[−19]	1.86[−17]	1.35[−17]	1.50[−18]	1.24[−17]	7.08[−18]	1.40[−18]	6.02[−18]
50	1.55[−17]	1.83[−18]	1.46[−17]	1.06[−17]	1.89[−18]	9.41[−18]	5.26[−18]	1.38[−18]	4.32[−18]
55	1.26[−17]	2.37[−18]	1.15[−17]	8.32[−18]	2.04[−18]	7.19[−18]	4.01[−18]	1.31[−18]	3.20[−18]
60	1.02[−17]	2.67[−18]	9.15[−18]	6.66[−18]	2.06[−18]	5.65[−18]	3.15[−18]	1.23[−18]	2.47[−18]
65	8.49[−18]	2.80[−18]		5.47[−18]	2.03[−18]		2.55[−18]	1.16[−18]	
70	7.25[−18]	2.86[−18]		4.62[−18]	1.99[−18]		2.13[−18]	1.10[−18]	
75	6.37[−18]	2.87[−18]		4.01[−18]	1.96[−18]		1.81[−18]	1.06[−18]	
80	5.76[−18]	2.88[−18]		3.56[−18]	1.93[−18]		1.58[−18]	1.03[−18]	
85	5.34[−18]	2.90[−18]		3.23[−18]	1.92[−18]		1.40[−18]	1.00[−18]	
90	5.06[−18]	2.90[−18]		2.99[−18]	1.92[−19]		1.27[−18]	9.88[−19]	
95	4.88[−18]	2.93[−18]		2.81[−18]	1.93[−18]		1.17[−18]	9.76[−19]	
100	4.76[−18]	2.96[−18]		2.68[−18]	1.94[−18]		1.09[−18]	9.69[−19]	
105	4.70[−18]	2.10[−18]		2.59[−18]	1.97[−18]		1.03[−18]	9.66[−19]	
110	4.67[−18]	3.04[−18]		2.52[−18]	1.99[−18]		9.81[−19]	9.65[−19]	
115	4.66[−18]	3.09[−18]		2.48[−18]	2.02[−18]		9.46[−19]	9.67[−19]	
120	4.67[−18]	3.15[−18]		2.45[−18]	2.05[−18]		9.19[−19]	9.70[−19]	
125	4.70[−18]	3.20[−18]		2.43[−18]	2.08[−18]		8.99[−19]	9.75[−19]	
130	4.72[−18]	3.25[−18]		2.42[−18]	2.11[−18]		8.85[−19]	9.81[−19]	
135	4.76[−18]	3.30[−18]		2.42[−18]	2.14[−18]		8.75[−19]	9.87[−19]	
140	4.79[−18]	3.35[−18]		2.42[−18]	2.17[−18]		8.68[−19]	9.93[−19]	
145	4.83[−18]	3.39[−18]		2.43[−18]	2.19[−18]		8.64[−19]	1.00[−18]	
150	4.86[−18]	3.43[−18]		2.44[−18]	2.21[−18]		8.63[−19]	1.01[−18]	
155	4.89[−18]	3.47[−18]		2.45[−18]	2.23[−18]		8.65[−19]	1.01[−18]	
160	4.92[−18]	3.50[−18]		2.47[−18]	2.25[−18]		8.69[−19]	1.02[−18]	
165	4.95[−18]	3.52[−18]		2.49[−18]	2.26[−18]		8.75[−19]	1.02[−18]	
170	4.97[−18]	3.54[−18]		2.50[−18]	2.27[−18]		8.81[−19]	1.02[−18]	
175	4.98[−18]	3.55[−18]		2.51[−18]	2.28[−18]		8.85[−19]	1.02[−18]	
180	4.99[−18]	3.55[−18]		2.51[−18]	2.28[−18]		8.86[−19]	1.02[−18]	

sults of Mathur *et al.*, one can conclude that target polarization is a small effect for the $^3S \rightarrow {}^3P$ transition at these electron energies.

2. $2\,^3S \rightarrow 3\,^3S, 3\,^3D$

Figure 4 compares the experimental results of Müller-Fielder *et al.* [9], for excitation from the $2\,^3S$ state to the $3\,^3S$ and $3\,^3D$ states, for final electron energies of 15, 20, and 30 eV, with the DWA results of Mathur *et al.* [10] and the present DWA and FOMBT(1) results.

The comparisons for excitation of the $3\,^3S$ state in Fig. 4 lead to the following two interesting conclusions. First, as for the $2\,^3S \rightarrow 3\,^3P$ transition, target polarization appears to be a negligible physical effect because of the very

TABLE III. DCSs (cm^2/sr) for electron-impact excitation $2\,^3S \rightarrow 3\,^3P$ for scattered electron energies of 15, 20, and 30 eV. The present FOMBT(1) and DWA results are described in the text. The results from Mathur *et al.* are from Ref. [10]. The numbers in brackets denote multiplicative powers of 10.

Angle \ E(final)	15 eV			20 eV			30 eV		
(deg)	FOMBT(1)	DWA	Mathur *et al.*	FOMBT(1)	DWA	Mathur *et al.*	FOMBT(1)	DWA	Mathur *et al.*
0	1.39[−15]	1.33[−15]	1.22[−15]	2.06[−15]	1.95[−15]	1.88[−15]	3.46[−15]	3.27[−15]	3.29[−15]
1	1.33[−15]	1.27[−15]	1.16[−15]	1.92[−15]	1.82[−15]	1.74[−15]	3.00[−15]	2.85[−15]	2.84[−15]
2	1.16[−15]	1.12[−15]	1.00[−15]	1.56[−15]	1.49[−15]	1.40[−15]	2.09[−15]	1.99[−15]	1.94[−15]
3			8.02[−16]						
4	7.06[−16]	7.05[−16]	6.02[−16]	7.84[−16]	7.76[−16]	1.02[−15]	7.36[−16]	7.27[−16]	1.18[−15]
5			4.30[−16]						
6	3.48[−16]	3.73[−16]	2.96[−16]	3.12[−16]	3.33[−16]	6.88[−16]	2.00[−16]	2.17[−16]	6.65[−16]
7			1.96[−16]						
8	1.41[−16]	1.72[−16]	1.27[−16]	9.53[−17]	1.21[−16]	4.43[−16]	3.14[−17]	4.73[−17]	3.61[−16]
9			7.87[−17]						
10	4.15[−17]	6.85[−17]	4.77[−17]	1.59[−17]	3.47[−17]	2.74[−16]	1.82[−20]	7.81[−18]	1.86[−16]
12	5.38[−18]	2.31[−17]		1.07[−19]	9.22[−18]	1.64[−16]	1.16[−17]	1.168[−17]	8.97[−17]
14	1.07[−18]	9.19[−18]		8.77[−18]	9.56[−18]	9.33[−17]	2.85[−17]	2.36[−17]	3.94[−17]
15			1.20[−17]						
16	9.70[−18]	1.02[−17]		2.24[−17]	1.79[−17]	5.04[−17]	3.83[−17]	3.17[−17]	1.65[−17]
20	2.98[−17]	2.30[−17]	2.32[−17]	3.74[−17]	3.04[−17]	2.65[−17]	3.54[−17]	3.10[−17]	9.24[−18]
25	3.54[−17]	2.87[−17]	2.45[−17]	3.12[−17]	2.72[−17]		1.82[−17]	1.74[−17]	
30	2.64[−17]	2.19[−17]	1.77[−17]	1.77[−17]	1.59[−17]		6.80[−18]	6.92[−18]	
35	1.57[−17]	1.30[−17]	1.06[−17]	8.20[−18]	7.42[−18]	1.72[−17]	2.08[−18]	2.37[−18]	2.99[−17]
40	8.36[−18]	6.99[−18]	6.01[−18]	3.39[−18]	3.43[−18]		5.48[−19]	1.03[−18]	
45	4.28[−18]	3.89[−18]	3.51[−18]	1.34[−18]	1.85[−18]	2.89[−17]	1.28[−19]	6.35[−19]	2.90[−17]
50	2.25[−18]	2.35[−18]	2.22[−18]	5.49[−19]	1.14[−18]	2.32[−17]	3.73[−20]	4.14[−19]	1.51[−17]
55	1.30[−18]	1.56[−18]	1.49[−18]	2.69[−19]	7.64[−19]	1.34[−17]	3.03[−20]	2.81[−19]	6.12[−18]
60	8.66[−19]	1.11[−18]	1.01[−18]	1.81[−19]	5.48[−19]	6.63[−18]	3.99[−20]	2.12[−19]	2.42[−18]
65	6.72[−19]	7.89[−19]		1.64[−19]	3.84[1−9]	3.29[−18]	5.00[−20]	1.50[−19]	1.12[−18]
70	5.92[−19]	5.40[−19]		1.71[−19]	2.52[−19]	1.79[−18]	5.82[−20]	9.44[−20]	6.04[−19]
75	5.68[−19]	3.67[−19]		1.87[−19]	1.72[−19]	1.08[−18]	6.49[−20]	6.59[−20]	3.62[−19]
80	5.74[−19]	2.58[−19]		2.05[−19]	1.37[−19]	6.93[−19]	7.09[−20]	6.38[−20]	2.30[−19]
85	5.96[−19]	1.88[−19]		2.25[−19]	1.18[−19]	4.50[−19]	7.67[−20]	6.66[−20]	1.48[−19]
90	6.27[−19]	1.49[−19]		2.46[−19]	1.08[−19]		8.28[−20]	6.36[−20]	
95	6.65[−19]	1.42[−19]		2.67[−19]	1.10[−19]		8.92[−20]	5.88[−20]	
100	7.07[−19]	1.61[−19]		2.89[−19]	1.21[−19]		9.61[−20]	5.84[−20]	
105	7.51[−19]	1.94[−19]		3.12[−19]	1.37[−19]		1.03[−19]	6.46[−20]	
110	7.98[−19]	2.41[−19]		3.35[−19]	1.59[−19]		1.11[−19]	7.30[−20]	
115	8.45[−19]	3.03[−19]		3.58[−19]	1.90[−19]		1.19[−19]	8.14[−20]	
120	8.92[−19]	3.71[−19]		3.82[−19]	2.19[−19]		1.27[−19]	8.40[−20]	
125	9.39[−19]	4.34[−19]		4.06[−19]	2.38[−19]		1.36[−19]	8.44[−20]	
130	9.85[−19]	4.95[−19]		4.29[−19]	2.55[−19]		1.44[−19]	8.85[−20]	
135	1.03[−18]	5.64[−19]		4.51[−19]	2.83[−19]		1.52[−19]	9.86[−20]	
140	1.07[−18]	6.36[−19]		4.72[−19]	3.16[−19]		1.59[−19]	1.08[−19]	
145	1.11[−18]	6.96[−19]		4.92[−19]	3.37[−19]		1.66[−19]	1.10[−19]	
150	1.14[−18]	7.37[−19]		5.09[−19]	3.43[−19]		1.73[−19]	1.07[−19]	
155	1.17[−18]	7.75[−19]		5.25[−19]	3.53[−19]		1.78[−18]	1.09[−19]	
160	1.20[−18]	8.23[−19]		5.38[−19]	3.80[−19]		1.83[−19]	1.20[−19]	
165	1.22[−18]	8.67[−19]		5.49[−19]	4.05[−19]		1.87[−19]	1.29[−19]	
170	1.23[−18]	8.82[−19]		5.56[−19]	4.02[−19]		1.89[−19]	1.25[−19]	
175	1.24[−18]	8.70[−19]		5.61[−19]	3.74[−19]		1.91[−19]	1.12[−19]	
180	1.25[−18]	8.60[−19]		5.63[−19]	3.58[−19]		1.92[−19]	1.05[−19]	

close agreement between the present DWA results and the DWA polarization results of Mathur *et al.* Second, distortion of the incident and scattered electrons by the fields of the initial and final excited states appears to be an important effect for ^3S-^3S transitions. This conclusion is based on the large difference in the predicted DCSs between the present DWA and FOMBT(1) results for scattering angles greater than 20° and the fact that results from DWA appear to agree better with experiment than do those from FOMBT(1). The deep minimum in the DCS predicted by FOMBT(1) is believed to be a result of the node in the $3\,^3S(3s)$ orbital required to ensure wavefunction orthogonality to the $2\,^3S$ wave function. It should be noted that, based on comparisons with previous studies [11], transitions to a particular final state from the metastable helium states appear to be much more sensitive to details of excited-state distortion than are excitations from the helium ground state.

The upper half of Fig. 4 shows a similar experimental-theoretical comparison for excitation of the $3\,^3D$ state from the $2\,^3S$ state, again at 15-, 20-, and 30-eV final electron energies. A comparison of the magnitudes of the DCSs in Figs. 3 and 4 reveals that excitation of the $3\,^3D$ state has the largest DCS of any transition at the three

TABLE IV. DCSs (cm^2/sr) for electron-impact excitation $2\,^3S \rightarrow 3\,^3D$ for scattered electron energies of 15, 20, and 30 eV. The present FOMBT(1) and DWA results are described in the text. The Born results are from the present paper. The numbers in brackets denote multiplicative powers of 10.

Angle \ E(final)	15 eV			20 eV			30 eV		
(deg)	FOMBT(1)	DWA	Born	FOMBT(1)	DWA	Born	FOMBT(1)	DWA	Born
0	1.35[−15]	1.28[−15]	1.35[−15]	1.44[−15]	1.40[−15]	1.42[−15]	1.53[−15]	1.53[−15]	1.50[−15]
1	1.35[−15]	1.27[−15]	1.34[−15]	1.43[−15]	1.38[−15]	1.41[−15]	1.51[−15]	1.50[−15]	1.49[−15]
2	1.32[−15]	1.24[−15]	1.32[−15]	1.40[−15]	1.34[−15]	1.39[−15]	1.46[−15]	1.43[−15]	1.45[−15]
4	1.25[−15]	1.15[−15]	1.26[−15]	1.29[−15]	1.22[−15]	1.30[−15]	1.31[−15]	1.26[−15]	1.32[−15]
6	1.13[−15]	1.04[−15]	1.16[−15]	1.14[−15]	1.07[−15]	1.16[−15]	1.10[−15]	1.05[−15]	1.12[−15]
8	9.95[−16]	9.09[−16]	1.03[−15]	9.71[−16]	9.06[−16]	1.00[−15]	8.78[−16]	8.38[−16]	9.03[−16]
10	8.49[−16]	7.76[−16]	8.88[−16]	7.93[−16]	7.41[−16]	8.27[−16]	6.60[−16]	6.32[−16]	6.86[−16]
12	7.02[−16]	6.44[−16]	7.43[−16]	6.23[−16]	5.86[−16]	6.58[−16]	4.70[−16]	4.54[−16]	4.95[−16]
14	5.64[−16]	5.21[−16]	6.05[−16]	4.72[−16]	4.47[−16]	5.06[−16]	3.19[−16]	3.11[−16]	3.41[−16]
16	4.41[−16]	4.10[−16]	4.80[−16]	3.46[−16]	3.31[−16]	3.77[−16]	2.07[−16]	2.05[−16]	2.25[−16]
20	2.50[−16]	2.38[−16]	2.82[−16]	1.70[−16]	1.68[−16]	1.92[−16]	7.84[−17]	8.33[−17]	8.88[−17]
25	1.09[−16]	1.10[−16]	1.29[−16]	6.08[−17]	6.71[−17]	7.27[−17]	1.99[−17]	2.79[−17]	2.41[−17]
30	4.32[−17]	5.06[−17]	5.41[−17]	1.95[−17]	2.88[−17]	2.49[−17]	4.61[−18]	1.25[−17]	5.90[−18]
35	1.62[−17]	2.59[−17]	2.11[−17]	6.03[−18]	1.54[−17]	8.01[−18]	1.21[−18]	7.52[−18]	1.36[−18]
40	6.13[−18]	1.60[−17]	7.92[−18]	2.04[−18]	1.03[−17]	2.48[−18]	5.46[−19]	5.17[−18]	3.06[−19]
45	2.60[−18]	1.16[−17]	2.89[−18]	9.49[−19]	7.58[−18]	7.51[−19]	4.30[−19]	3.66[−18]	6.72[−20]
50	1.41[−18]	8.98[−18]	1.05[−18]	6.71[−19]	5.73[−18]	2.26[−19]	4.01[−19]	2.60[−18]	1.43[−20]
55	1.01[−18]	7.13[−18]	3.76[−19]	5.99[−19]	4.34[−18]	6.75[−20]	3.79[−19]	1.85[−18]	2.85[−21]
60	8.71[−19]	5.68[−18]	1.36[−19]	5.73[−19]	3.28[−18]	2.00[−20]	3.54[−19]	1.33[−18]	4.90[−22]
65	8.18[−19]	4.49[−18]	4.92[−20]	5.54[−19]	2.48[−18]	5.80[−21]	3.27[−19]	9.62[−19]	5.62[−23]
70	7.93[−19]	3.54[−18]	1.78[−20]	5.36[−19]	1.87[−18]	1.61[−21]	3.02[−19]	7.06[−19]	6.60[−25]
75	7.79[−19]	2.77[−18]	6.42[−21]	5.19[−19]	1.41[−18]	4.04[−22]	2.80[−19]	5.19[−19]	4.26[−24]
80	7.69[−19]	2.16[−18]	2.27[−21]	5.03[−19]	1.07[−18]	8.16[−23]	2.61[−19]	3.87[−19]	9.81[−24]
85	7.63[−19]	1.67[−18]	7.76[−22]	4.91[−19]	8.14[−19]	8.64[−24]	2.45[−19]	2.96[−19]	1.13[−23]
90	7.59[−19]	1.30[−18]	2.45[−22]	4.81[−19]	6.27[−19]	1.26[−25]	2.33[−19]	2.32[−19]	1.04[−23]
95	7.58[−19]	1.01[−18]	6.63[−23]	4.76[−19]	4.96[−19]	4.30[−24]	2.25[−19]	1.89[−19]	8.66[−24]
100	7.60[−19]	8.17[−19]	1.23[−23]	4.74[−19]	4.14[−19]	8.46[−24]	2.20[−19]	1.65[−19]	6.90[−24]
105	7.65[−19]	7.00[−19]	4.30[−25]	4.75[−19]	3.71[−19]	1.06[−23]	2.19[−19]	1.56[−19]	5.39[−24]
110	7.72[−19]	6.52[−19]	1.17[−24]	4.80[−19]	3.61[−19]	1.10[−23]	2.21[−19]	1.56[−19]	4.19[−24]
115	7.81[−19]	6.63[−19]	4.50[−24]	4.89[−19]	3.80[−19]		2.26[−19]	1.65[−19]	
120	7.92[−19]	7.26[−19]	7.42[−24]	5.00[−19]	4.25[−19]	9.70[−24]	2.34[−19]	1.84[−19]	2.59[−24]
125	8.04[−19]	8.36[−19]	9.34[−24]	5.14[−19]	4.91[−19]		2.44[−19]	2.08[−19]	
130	8.17[−19]	9.85[−19]	1.04[−23]	5.30[−19]	5.71[−19]	7.74[−24]	2.55[−19]	2.34[−19]	1.68[−24]
135	8.31[−19]	1.16[−18]		5.47[−19]	6.63[−19]		2.68[−19]	2.67[−19]	
140	8.45[−19]	1.36[−18]	1.08[−23]	5.65[−19]	7.63[−19]	6.14[−24]	2.82[−19]	3.02[−19]	1.17[−24]
145	8.590[−19]	1.563[−18]		5.83[−19]	8.62[−19]		2.96[−19]	3.35[−19]	
150	8.721[−19]	1.762[−18]	1.03[−23]	6.00[−19]	9.57[−19]	5.02[−24]	3.09[−19]	3.69[−19]	8.82[−25]
155	8.841[−19]	1.947[−18]		6.16[−19]	1.05[−18]		3.21[−19]	4.01[−19]	
160	8.844[−19]	2.114[−18]	9.62[−24]	6.30[−19]	1.13[−18]	4.31[−24]	3.32[−19]	4.23[−19]	7.19[−25]
165	9.028[−19]	2.255[−18]		6.41[−19]	1.20[−18]		3.41[−19]	4.44[−19]	
170	9.090[−19]	2.360[−18]	9.18[−24]	6.50[−19]	1.25[−18]	3.92[−24]	3.47[−19]	4.65[−19]	6.36[−25]
175	9.128[−19]	2.424[−18]		6.55[−19]	1.28[−18]		3.51[−19]	4.71[−19]	
180	9.141[−19]	2.446[−18]	9.026[−24]	6.57[−19]	1.30[−18]	3.80[−24]	3.53[−19]	4.70[−19]	6.11[−25]

electron energies used in the experiments.

The fact that all four models used for these transitions, ranging in sophistication from Born to DWA polarization, predict the same small-angle DCS and agree with the measured DCS indicates that direct excitation is the dominant physical effect for determining the magnitude of the integral cross section. However, experimental data at scattering angles out to at least 90° are needed in order to determine the relative importance of exchange and higher-order (e.g., polarization) effects. Because the four transitions discussed above are the only ones for which experimental DCS data have been reported [10], the corresponding DWA and FOMBT(1) from this study are summarized in Tables I–IV at the same electron energies used in the experimental work. In Tables I–III the augmented DWA results of Mathur *et al.* [10] have also been included since they have not been reported previously in tabular form. A more comprehensive discussion of the systematics of the DCSs for excitation to higher states of different symmetry from these two metastable states will be given in a subsequent paper.

B. Integral cross sections

This section contains comparisons between integral cross-section results from various theoretical models and the available experimental data. Before discussing the graphic comparisons of the integral cross sections, we present numerical comparisons among various models and experiment where available, at a few selected incident electron energies in order to illustrate quantitatively the effect of incorporating various physical interactions in the excitation process.

Table V contains a comparison of the FOMBT(1) and FOMBT(2) integral cross sections with those predicted by the five-state R-matrix [18], the polarized DWA [10], and the Born approximation models for the $2\,^3S \rightarrow 2\,^3P$ transition. As shown in the table, the FOMBT(2) results (that incorporate channel coupling to the ground state) are only slightly larger than those from FOMBT(1) (distorted-wave level), which agrees very well with the polarized DWA results of Mathur *et al.* [10]. The fact that the FOMBT(1) and FOMBT(2) results are so close indicates that channel coupling to the ground state is relatively unimportant for strong dipole-allowed transitions such as this one.

Table VI contains a numerical comparison of FOMBT(1) and FOMBT(2) results for the two transitions $2\,^3S \rightarrow 3\,^3S, 3\,^3D$ with experiment [17] and those from polarized DWA [10] and 11-state R-matrix theory [19] at three electron energies. For this pair of transitions, FOMBT(2) predicts cross sections that are 30% larger than those from FOMBT(1) at low energies, which indicates that channel coupling to the ground state is more important for dipole-forbidden than for dipole-allowed transitions. It is difficult to make quantitative comparisons with the experimental results, except to note that they are larger (except at 6 eV) than predicted by these models, which is consistent with the fact that these "apparent" excitation cross sections contain undetermined cascade contributions from higher states.

Table VII contains a numerical comparison of the results from the FOMBT(1) and FOMBT(2) models for the dipole-allowed transition $2\,^3S \rightarrow 3\,^3P$ with the apparent excitation results of Rall *et al.* [17] and results from polarized DWA [10] and 11-state R-matrix scattering models. The comparison of FOMBT(1) and FOMBT(2) again shows that channel coupling to the ground state is relatively unimportant. It is also interesting to note that, for this particular transition, FOMBT(2) predicts integral cross sections which are substantially greater than those estimated by FOMBT(1).

Figures 5–9 compare the present integral cross-section results with a variety of experimental and theoretical results reported previously. In all these figures, excitation from the ground state of helium to the same final state is also shown to give the reader a clear picture as to both the greater magnitudes and different energy dependence for excitation from the helium metastable states.

TABLE V. Integral cross sections (10^{-16} cm^2) for the electron-impact-induced $2\,^3S \rightarrow 2\,^3P$ transition in helium.

Final electron energy (eV)	Five-state R matrix[a]	Polarized DWA[b]	FOMBT(1)[c]	FOMBT(2)[d]	Born e	Born f
9.49	87.94		107.2	111.6		107.5
10		99.71	103.6	107.5	104.3	103.9
20		64.47	64.30	65.03	63.87	64.55
30		48.09	47.45	47.76	47.86	47.60
60.711	29.14		26.73	26.80		26.81
79.081	23.73		21.34	21.38		21.40

[a]Fon *et al.* [18].
[b]Mathur *et al.* [10].
[c]Present results with distorted-wave terms only.
[d]Present results with channel coupling included.
[e]Born results of Ton-That, Manson, and Flannery [12].
[f]Present Born results.

TABLE VI. Integral cross sections (10^{-16} cm^2) for the electron-impact-induced $2\,^3S \rightarrow 3\,^3S, 3\,^3P$ transitions in helium. The asterisk denotes the results for $E = 15$ eV incident electron energy.

Incident electron energy (eV)	Experiment[a]		11-state R matrix[b]		Polarized DWA[c]	FOMBT(1)[d]		FOMBT(2)[e]	
	$3\,^3S$	$3\,^3D$	$3\,^3S$	$3\,^3D$	$3\,^3S$	$3\,^3S$	$3\,^3D$	$3\,^3S$	$3\,^3D$
6	<8.1	>11.0	2.99	5.37		5.90	18.76	7.70	24.20
10	<4.8	>8.0	2.29	6.33	2.29	2.58	5.48	3.01	6.40
16	<2.4	>4.9			1.95*	1.75	3.51	1.86	3.73

[a]Rall *et al.* [17].
[b]Berrington *et al.* [19].
[c]Mathur *et al.* [10].
[d]Present results with distorted-wave terms only.
[e]Present results with channel-coupling included.

1. $2\,^3S \rightarrow 2\,^3P$ and $2\,^1S \rightarrow 2\,^1P$

Figure 5 shows integral excitation cross sections, as a function of the incident electron energy, for the "spin-conserving" $2\,^3S \rightarrow 2\,^3P$ and $2\,^1S \rightarrow 2\,^1P$ excitation processes. No experimental results have been reported for these two transitions, so the comparisons in this figure are for results from different theoretical models. Note that the integral cross section for the $2\,^1S \rightarrow 2\,^1P$ excitation is predicted to be roughly a factor of 2 larger than that for the $2\,^3S \rightarrow 2\,^3P$ excitation.

It should be noted that, for these two transitions, all the theoretical models (including Born) predict about the same magnitude and energy dependence of the integral cross section for incident electron energies of 30 eV and greater. Because the sophistication of the theoretical models represented in Fig. 5 range from those without exchange [Born and multichannel eikonal theory (MCE) [12,13]] to DWA polarization (i.e., full direct and exchange distortion plus target polarization), one must conclude that the magnitude and shape of the integral cross sections for these spin-conserving transitions are dominated by the "direct" excitation, for energies greater than about 15 eV. However, for incident electron energies less than about 15 eV, results from the different theoretical models diverge from each other. The energy dependence predicted by the 19-state [14] and 29-state [15] R-matrix models shows large oscillations, but is substantially lower than that predicted by other models closest to those theories which include some target polarization (Badnell [16] and MCE [13]). The simplest conclusion to draw from this comparison is that at these lower energies (i.e., for energies *less* than Müller-Fiedler used in measuring the DCSs), target polarization reduces the integral cross sections by about a factor of 2. Correspondingly, those theoretical models which do not incorporate some target polarization (Born and DWA) appear to overestimate the integral cross section by about a factor of 2 for incident electron energies less than about 10 eV. This result is not surprising because the Born and DWA scattering models are based on a "weak-coupling" approximation. In fact, it is somewhat surprising that the DWA and Born models work as well as they do for incident electron energies as low as 20 eV. We offer no explanation for why the results from the 19- and 29-state R-matrix calculations have such different shapes for the

TABLE VII. Integral cross sections (10^{-16} cm^2) for the electron-impact-induced $2\,^3S \rightarrow 3\,^3P$ transition in helium.

Incident electron energy (eV)	Experiment[a]	11-state R matrix[b]	Polarized DWA[c]	No-exchange FOMBT(1)	FOMBT(1)[d]	FOMBT(2)[e]	Born[f]
4.5	3.1	2.5		1.19	32.10	38.60	1.48
6.0	3.0	2.2			14.30	17.60	
10.0	2.1		0.67		2.30	2.90	
16.0	1.7		0.60		0.85	0.98	

[a]Rall *et al.* [17].
[b]Berrington *et al.* [19].
[c]Mathur *et al.* [10].
[d]Present results with distorted-wave terms only.
[e]Present results with channel coupling included.
[f]Present results.

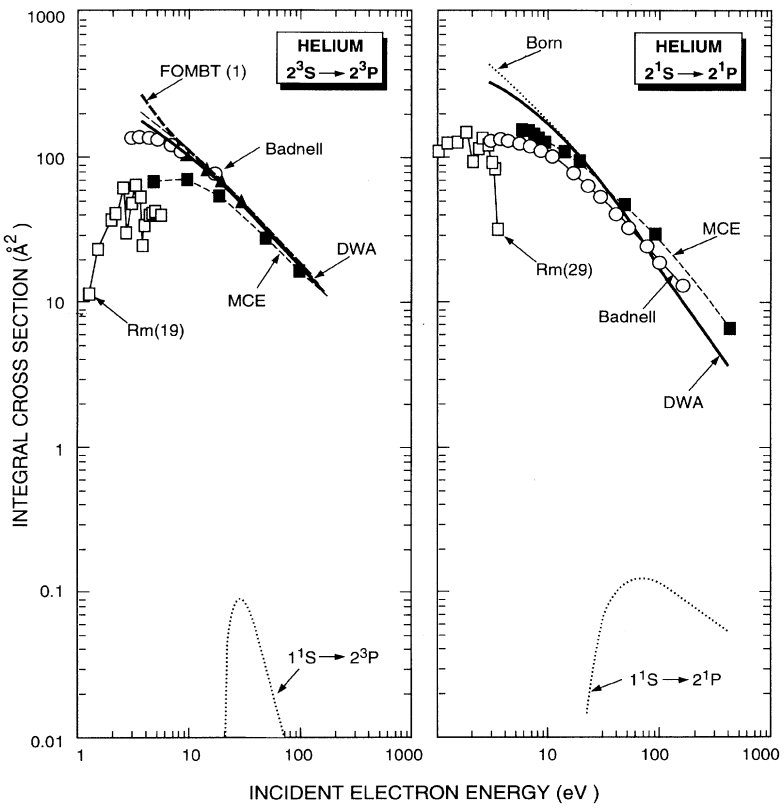

FIG. 5. Integral cross sections (10^{-16} cm^2) for the excitation processes $2\,^3S \rightarrow 2\,^3P$ (left panel) and $2\,^1S \rightarrow 2\,^1P$ (right panel). Also shown in the lower part of each panel for purposes of comparison is the corresponding excitation from the helium ground state. In addition to the FOMBT(1), DWA, and Born results from the present study, the (19-state and 29-state) R-matrix results from Fon, Berrington, and Kingston [14(b),14(c)] are shown along with the results from Badnell [16] and the MCE [13] scattering model.

two sets of transitions in Fig. 5 or why the results from Badnell are qualitatively different relative to the Born and DWA results for the two (presumably similar) sets of transitions.

2. $2\,^3S \rightarrow 3\,^3S, 3\,^3P, 3\,^3D$

Figure 6 compares experimental and theoretical integral cross sections for the $2\,^3S \rightarrow 3\,^3S$, $3\,^3P$, and $3\,^3D$ transition in helium. For all three transitions, the only experimental data are the apparent excitation cross section results from Rall *et al.* [17], which are denoted as shaded regions in Fig. 6.

The apparent integral cross sections for excitation to a particular final state in Fig. 6 were determined by measuring the relative intensity of radiation from the state of interest, subtracting the cascade contribution from higher electronic states, and making the result absolute by a normalization process. These apparent excita-

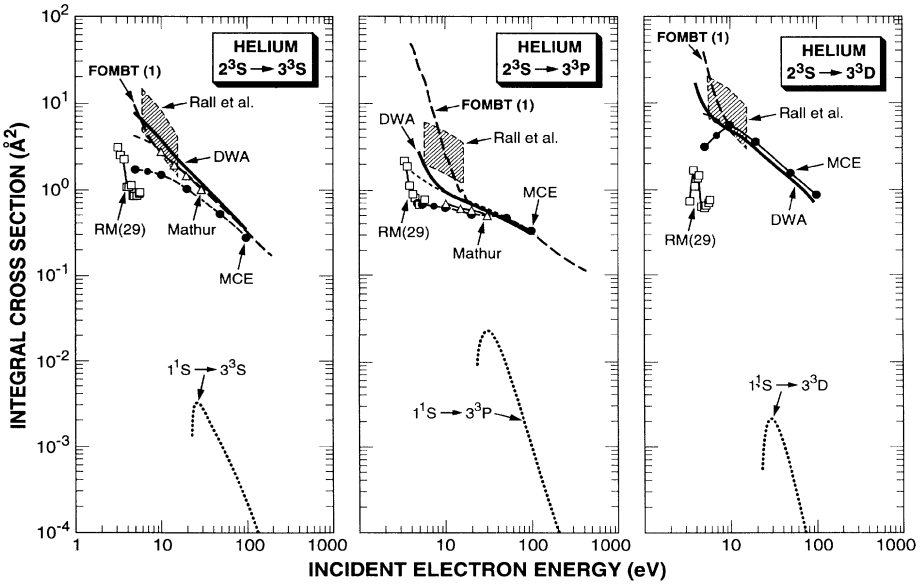

FIG. 6. Integral cross sections (10^{-16} cm^2) for excitation from the $2\,^3S$ metastable state to $3\,^3S$ (left panel), $3\,^3P$ (middle panel), and $3\,^3D$ (right panel). The vertical limits of the shaded regions denote the error range in the apparent excitation results from Rall *et al.* [17]. FOMBT(1), DWA, and Born results from the present study are shown along with 29-state R-matrix results [14(c)] the DWA model of Mathur *et al.* [10], and the MCE model [13].

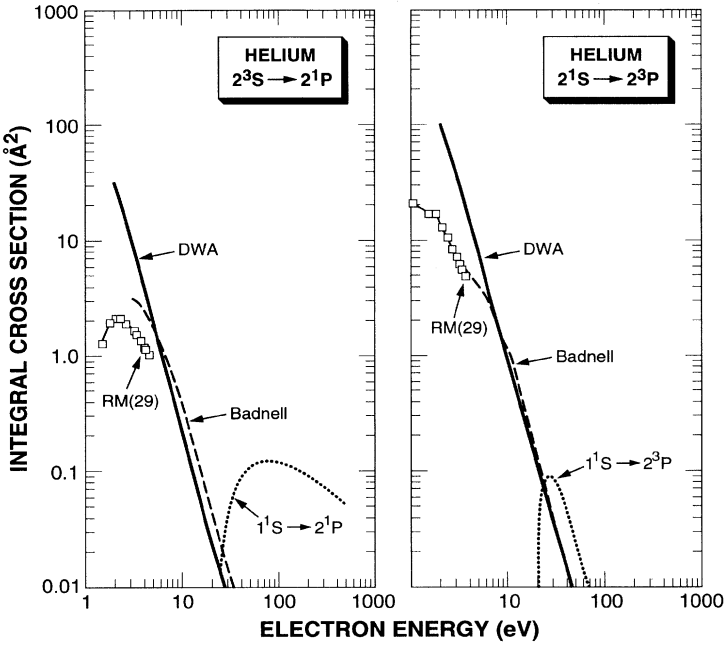

FIG. 7. Integral cross sections (10^{-16} cm^2) versus incident electron energy, for $2\,^3S \rightarrow 2\,^1P$ and $2\,^1S \rightarrow 2\,^3P$ excitation. The modified DWA results of Badnell and the 29-state R-matrix results [14(c)] are compared with the present DWA results. Also shown for comparison is excitation to the same final state from the ground ($1\,^1S$) helium state.

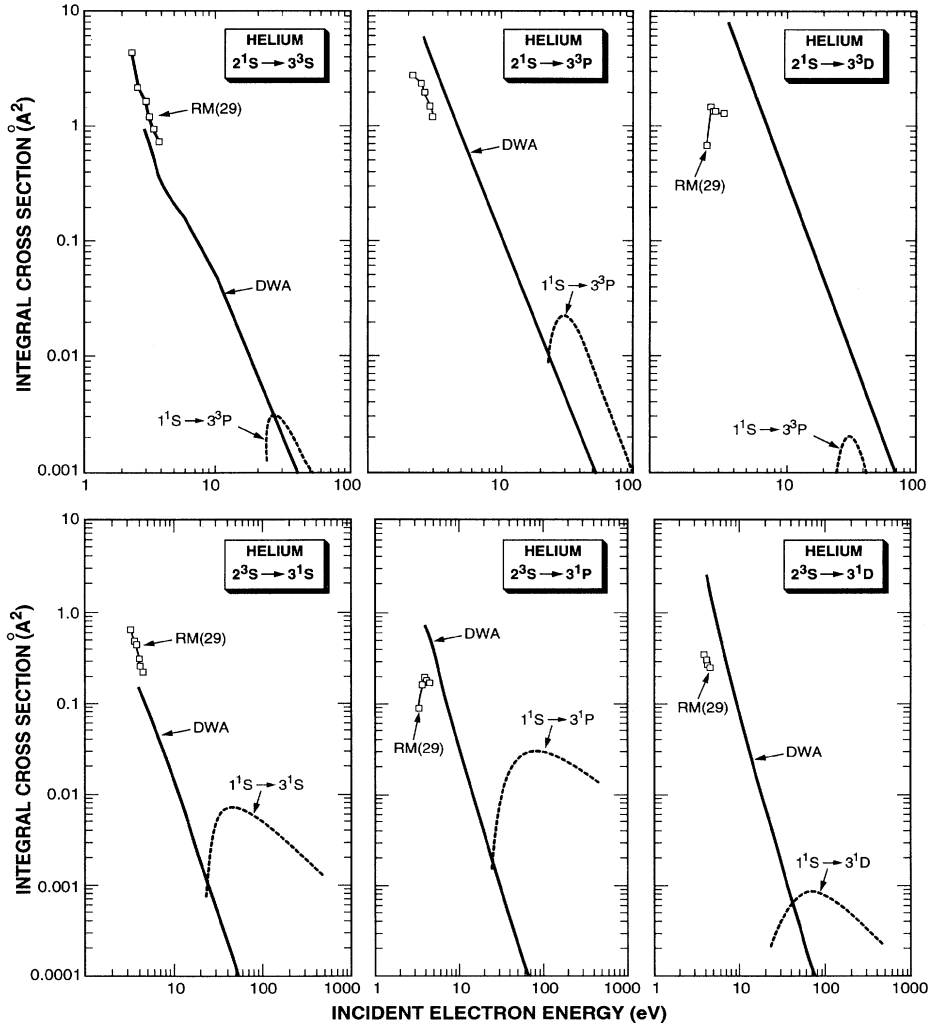

FIG. 8. Integral cross sections (10^{-16} cm^2) versus incident electron energy, for the $2\,^3S \rightarrow 3\,^1S, 3\,^1P$, and $3\,^1D$ excitation processes in the lower half of the figure and $2\,^1S \rightarrow, 3\,^3S, 3\,^3P$, and $3\,^3D$ in the upper half. The present DWA results are shown as the heavy solid lines and the 29-state R-matrix results as the open squares. No experimental results have been reported for these transitions. Excitation from the ground state of helium ($1\,^1S$) is shown as the light dotted line in each panel to illustrate the differences in magnitudes and energy dependence.

tion cross sections are generally "upper limits" to the true excitation cross sections because of the difficulty in quantitatively accounting for all the cascade contributions from higher atomic states.

Key points that should be emphasized from the comparisons in Fig. 6 are the following. As mentioned in Sec. III A dealing with the DCSs, the integral cross section for excitation of the $3\,^3D$ state is indeed the largest, as predicted to be the case by all theoretical models except R-matrix theory. An explanation for why the R-matrix model predicts the $3\,^3D$ integral cross section to be the smallest of the three in Fig. 6 is not offered here. It is also noted that, in general, the R-matrix theory integral sections are the smallest of those predicted by any of the theories and substantially smaller than experiment. All models except R-matrix theory appear to predict similar integral cross sections, in both magnitude and shape, for incident electron energies greater than almost 20 eV. However, for energies less than almost 20 eV, there are substantial differences in the predicted integral cross sections. In general, the FOMBT(1) model predicts the largest cross section from the metastable initial state below 20 eV, while the *augmented* DWA models (Badnell [16] and Mathur *et al.* [10]) predict the smallest. The present Born, the DWA, and the MCE models predict integral cross sections in between these results. As shown in Fig. 6, the integral cross sections predicted by the present FOMBT(1), DWA, and Born models increase sharply for energies below about 10 eV for the $2\,^3S \rightarrow 3\,^3P$ and $3\,^3D$ transitions, in seemingly better agreement with the results of Rall *et al.* [17]. However, the better agreement shown in Fig. 6 may be fortuitous because of the upper limit nature of the experimental results mentioned above. It is worth noting that the integral cross sections in Fig. 6 for excitation from the $2\,^3S$ state range from 20 to 1000 times larger than that for excitation from the ground state.

3. *Pure exchange transitions: $2\,^3S \rightarrow 2\,^1P$ and $2\,^1S \rightarrow 2\,^3P$*

Figure 7 compares three sets of theoretical integral cross sections for the purely exchange transitions $2\,^3S \rightarrow 2\,^1P$ and $2\,^1S \rightarrow 2\,^3P$. No experimental results have been reported for these transitions. Also shown in each panel is the excitation cross section to the same final state from the ground ($1\,^1S$) state in helium. The comparisons in this figure show that the 29-state R-matrix theory results are somewhat smaller than the results from the other theoretical models. In the case of $2\,^1P$ as the final state, excitation from the ground state is spin allowed, which explains why the cross section for excitation from the ground state falls off more slowly with increasing electron energy. It is noted here that the MCE model predicts an identically zero cross section for these "spin-forbidden" excitation processes because this model does not include electron exchange.

4. *Pure exchange transitions: $2\,^3S \rightarrow 3\,^1S, 3\,^1P, 3\,^1D$ and $2\,^1S \rightarrow 3\,^3S, 3\,^3P, 3\,^3D$*

Integral excitation cross sections from the $2\,^3S$ and $2\,^1S$ metastable states to the $3\,^{1,3}S$, $3\,^{1,3}P$, and $3\,^{1,3}D$ states are shown in Fig. 8. As in the other figures, excitations from the helium ground state to the same final state is also shown for comparison purposes. No experimental integral cross section data have been reported to which comparisons can be made. The R-matrix theory results are slightly larger than those from the present DWA model for the $2\,^3S \rightarrow 3\,^1S, 3\,^3S$ excitations, but smaller than the DWA results for the P and D symmetry excitations. It is interesting to note that the integral cross section for the pure exchange excitation processes $2\,^3S \rightarrow 3\,^1D$ and $2\,^1S \rightarrow 3\,^3D$ are predicted to be the largest for excitation of the $n = 3$ manifold in contrast to that for excitation from the ground state of helium. Agreement between the R-matrix and present DWA results is reasonably good, although the R-matrix model appears to predict too small a cross section for excitation to the $3\,^3D$ state. As in the other pure exchange transition the MCE model predicts a zero excitation cross section because it neglects the exchange interaction. Note the key large differences in magnitude and energy dependence between excitation from the metastable state and that for excitation from the ground state of helium.

Figure 9 provides a "global" comparison of the integral cross sections (10^{-16} cm^2), as a function of incident electron energy (eV), for excitation from the $2\,^{1,3}S$ metastable states to a few selected final states in helium with the sum of integral cross sections for excitation to *all* final helium bound states. For comparison the lower right-hand portion of this figure shows the sum of integral cross sections for excitation to all bound states in

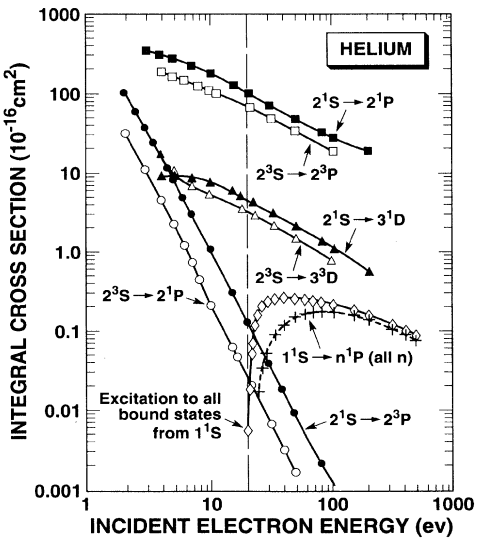

FIG. 9. Integral cross sections (10^{-16} cm^2), as a function of incident electron energy (eV), for excitation from the $2\,^3S$ and $2\,^1S$ metastable states to selected final states indicated in the figure. In the lower right-hand portion of the figure the sum of integral cross sections for excitation from the helium ground state to *all* final $n\,^1P$ states and to *all* bound states are shown (+ and − symbols and open triangles, respectively) to illustrate differences in the magnitudes and energy dependence. The vertical dashed line denotes the lowest inelastic threshold for excitation from the helium ground state.

helium from the ground states as open triangles connected by the solid line. The plus symbols connected by the dashed line in the lower right-hand portion of this figure denote the sum of integral cross sections for excitation of all the $n\ ^1P$ states from the ground state of helium. The vertical dashed line denotes the lowest-energy threshold for excitation from the ground state. This comparison illustrates two important characteristics of the integral cross sections for excitation from the metastable states that are important for modeling helium plasmas: (i) excitation from the metastable states to a specific final state is substantially greater than that from the ground state and (ii) the integral cross sections for excitation from the metastable states is largest for electron energies below 20 eV, where the cross sections for excitation from the ground state is identically zero. Since the electron distribution function in most practical plasma environments increases exponentially as the energy decreases below 20 eV, the increasing cross sections for excitation from the metastable states means that inelastic processes involving these two metastable states may play a very important role in most partially ionized plasmas, as recently reported by Alves, Gousset, and Ferrevia [21]. The systematic behavior of the cross sections for excitation from these two metastable states, as well as an estimate of the total scattering cross sections for excitation from these two metastable states, will be reported in a subsequent publication.

ACKNOWLEDGMENTS

The authors want to acknowledge the financial support of the U.S. DOE, the NSF (OIP), and the CNPq of Brazil. This work was also part of the CALCOR program, a collaborative research program between the University of California (UC Riverside) and Los Alamos National Laboratory. The authors also thank Professor McEachran and Professor Stauffer for providing data for the results reported in Ref. [10] (given here in Tables I–III) and Professor Takashi Fujimoto (Kyoto University) for providing helpful comments which improved the quality of this paper.

[1] G. Csanak, D. C. Cartwright, and F. J. da Paixão, Phys. Rev. A **48**, 2811 (1993).
[2] G. Bates, Comput. Phys. Commun. **8**, 220 (1974).
[3] C. S. Sharma and C. A. Coulson, Proc. Phys. Soc. London **80**, 81 (1962).
[4] M. Cohen and R. P. McEachran, Proc. Phys. Soc. London **92**, 37 (1967).
[5] R. P. McEachran and M. Cohen, J. Phys B **2**, 1271 (1969).
[6] D. S. F. Crothers and R. P. McEachran, J. Phys. B **3**, 976 (1970).
[7] G. N. Bates, Comput. Phys. Commun. **8**, 320 (1974).
[8] A. R. Edmonds, *Angular Momentum in Quantum Mechanics* (Princeton University Press, Princeton, 1957).
[9] R. Müller-Fiedler, P. Schlemmer, K. Jung, H. Hotop, and H. Ehrhardt, J. Phys. B **17**, 259 (1984).
[10] K. C. Mathur, R. P. McEachran, L. A. Parcell, and A. D. Stauffer, J. Phys. B **20**, 1599 (1987).
[11] D. C. Cartwright, G. Csanak, S. Trajmar, and D. F. Register, Phys. Rev. A **45**, 1602 (1992); S. Trajmar, D. F. Register, D. C. Cartwright, and G. Csanak, J. Phys. B **25**, 4889 (1992).
[12] D. Ton-That, S. T. Manson, and M. R. Flannery, J. Phys. B **10**, 621 (1977).
[13] M. R. Flannery and K. J. McCann, Phys. Rev. A **12**, 846 (1976); E. J. Mansky and M. R. Flannery, J. Phys. B **25**, 1591 (1992).
[14] (a) K. A. Berrington, W. C. Fon, L. C. Freitas, and A. E. Kingston, J. Phys. B **20**, L685 (1987); (b) W. C. Fon, K. A. Berrington, and A. E. Kingston, *ibid.* **21**, 2961 (1988); (c) *ibid.* **24**, 2161 (1991).
[15] P. M. J. Sawey, K. A. Berrington, P. G. Burke, and A. E. Kingston, J. Phys. B **23**, 4321 (1990).
[16] N. R. Badnell, J. Phys. B **17**, 4013 (1984).
[17] D. L. A. Rall, F. A. Sharpton, M. B. Schulman, L. W. Anderson, J. E. Lawler, and C. C. Lin, Phys. Rev. Lett. **62**, 2253 (1989).
[18] W. C. Fon, K. A. Berrington, P. G. Burke, and A. E. Kingston, J. Phys. B **14**, 2921 (1981).
[19] K. A. Berrington, P. G. Burke, L. C. G. Freitas, and A. E. Kingston, J. Phys. B **18**, 4135 (1985).
[20] L. L. Alves, G. Gousset, and C. M. Ferrevia, J. Phys. D **25**, 1713 (1992).